Physics – Uspekhi **44** (6) 553 – 570 (2001)

© 2001 Uspekhi Fizicheskikh Nauk, Russian Academy of Sciences

REVIEWS OF TOPICAL PROBLEMS

PACS numbers: **64.75.+g**, **71.27.+a**, **72.10.–d**, 75.30.Vn

Inhomogeneous charge distributions and phase separation in manganites

M Yu Kagan, K I Kugel'

DOI: 10.1070/PU2001v044n06ABEH000917

Contents

1. **Introduction** 553
2. **Basic theoretical model** 554
3. **Low-doping case** 554
   3.1 Stability of a homogeneous state; 3.2 The energy of a state with ferromagnetic polarons within an antiferromagnetic matrix; 3.3 Electron – hole symmetry of the phase diagram of a ferromagnetic Kondo lattice
4. **Role of the Coulomb interaction between electrons** 558
   4.1 Charge ordering at densities $n \to 1/2$; 4.2 Stability of a charge-ordered state at densities close to $n = 1/2$; 4.3 The simplest example of phase separation in the Verwey model at densities $n < 1/2$; 4.4 Phase separation in the basic model of the ferromagnetic Kondo lattice with a Coulomb interaction for densities close to $n = 1/2$; 4.5 'Temperature' ferrons
5. **Phase separation in layered manganites** 564
   5.1 A canted state in layered manganites; 5.2 Magnetic polarons in layered manganites
6. **Transport properties of phase-separated manganites** 566
   6.1 Resistance in the percolation regime in phase-separated manganites; 6.2 Magnetoresistance in phase-separated manganites; 6.3 $1/f$ noise in phase-separated manganites
7. **Summary** 569
References 569

Abstract. **Mechanisms of electron phase separation in manganite-type oxide materials are analyzed using a simple Kondo-lattice model with intersite Coulomb repulsion between electrons. This model predicts the instability of magnetic (or charge) homogeneous ordering toward the formation of droplet structures (magnetic polarons) for a wide parameter range in the phase diagram. Various types of magnetic polarons are examined. The transport properties and noise spectrum of phase-separated materials are also discussed.**

1. Introduction

Manganites, the Mn-based magnetic oxide materials typified by $LaMnO_3$, have been under investigation for more than 50 years [1, 2] but attracted particular attention after the discovery in 1994 of the colossal magnetoresistance effect first observed for Ca-doped $LaMnO_3$ films [3]. There is currently considerable review literature on these materials (see, e.g., Refs [4 – 8]), and it is worthwhile noting that in Ref. [7] a bibliography of more than 600 references is given. This large body of original and review literature is due in part to the potential technological applications of colossal magnetoresistance, but also reflects the manganites' suitability for studying the physics of strongly correlated systems. In particular, the interaction of spin, charge, and orbital degrees of freedom in these materials as well as their rich phase diagrams are of interest. On the other hand, the possibility of various types of inhomogeneous charge and spin states in manganites — lattice and magnetic polarons, droplet and stripe structures, etc. — is currently receiving special attention.

Similar phenomena occur in many strongly correlated systems, where the potential energy of the interaction of electrons exceeds their kinetic energy. In particular, such phenomena are being widely discussed in connection with high-T_c superconductors (HTSC) [9 – 12]. Of earlier examples, ferromagnetic (FM) droplets (ferrons) in an antiferromagnetic (AFM) state at low doping levels [13, 14] and ferromagnetic spin polarons in a paramagnet [15, 16] (see also Ref. [17]) are particularly notable. A string (linear track of frustrated spins) created by a hole passing through an AFM insulator [18] should also be mentioned. All these phenomena are examples of the so-called electron phase separation effect, which results from individual charge carriers changing their local electron environment (it is favorable for such regions to be as far apart as possible to minimize the Coulomb energy). Along with this small-scale

---

M Yu Kagan P L Kapitza Institute for Physical Problems,
Russian Academy of Sciences
ul. Kosygina 2, 117334 Moscow, Russian Federation
Tel. (7-095) 137 79 85. Fax (7-095) 938 20 30
E-mail: kagan@kapitza.ras.ru
K I Kugel' Institute for Theoretical and Applied Electrodynamics,
Russian Academy of Sciences
Izhorskaya ul. 13/19, 127412 Moscow, Russian Federation
Tel. (7-095) 362 51 47. Fax (7-095) 484 26 33
E-mail: kugel@orc.ru

Received 13 December 2000, revised 4 April 2001
Uspekhi Fizicheskikh Nauk **171** (6) 577 – 596 (2001)
Translated by E G Strel'chenko; edited by S N Gorin

phase separation, manganites, as many other materials showing first-order transitions (between the AFM and FM phases, for example), display yet another type of phase separation, related to the fact that there is a large region of coexistence for various phases in the material. One example of such large-scale separation is the formation of relatively large FM droplets (100 – 1000 Å in size) in an AFM matrix [19, 20]. A noteworthy feature of manganites is the strong interaction between the electronic and lattice subsystems due to the fact that Mn^{3+} is a Jahn – Teller ion and therefore any phase separation gives rise to elastic lattice distortions which can be detected experimentally. Another characteristic feature is charge ordering, i.e., a regular arrangement of Mn^{3+} and Mn^{4+} ions, when the material in fact obtains an additional lattice period and hence acquires a superstructure. Along with a superstructure, nontrivial spin and orbital ordering may result from charge ordering. An example is the well-known zigzag magnetic structure (referred to usually as CE) in compounds of the type $\mathrm{Pr_{0.5}Ca_{0.5}MnO_3}$ [21, 22], in which charge ordering is accompanied by the formation of zigzag magnetic chains. The interaction of spin, charge, and orbital degrees of freedom can also lead to stripe [23] (rather than droplet) structures at high concentrations of an alkaline-earth element. Because of the strong interaction with the lattice, it turns out that in manganites (as opposed to HTSC systems) such structures are not dynamic but static and are observable with electron diffraction and X-ray small-angle scattering techniques.

In this paper, we will focus on the small-scale phase separation, in which the microscopic nature of charge transfer manifests itself most clearly. The outline of the paper is as follows: first, we analyze the low-doping case by addressing the ferromagnetic Kondo lattice — the basic model for manganites — with no Coulomb interaction between electrons on neighboring sites. We next allow for the Coulomb interaction and consider densities close to 1/2, a region where charge ordering is most likely. Based on the results thus obtained, the relation between the simplest phase separation models and the actual phase diagram of manganites is analyzed. In the last part of the review, the effects of phase separation on the transport properties are considered.

2. Basic theoretical model

The simplest theoretical model encompassing the basic physics of manganites is the ferromagnetic Kondo lattice ($s-d$ model) with a Coulomb interaction between conduction electrons:

$$\hat{H} = -J_{\mathrm{H}}\sum_{i}\mathbf{S}_i\,\boldsymbol{\sigma}_i - t\sum_{\langle ij\rangle} P c^{\dagger}_{i\sigma}c_{j\sigma}P + J_{ff}\sum_{\langle ij\rangle}\mathbf{S}_i\,\mathbf{S}_j + V\sum_{\langle ij\rangle} n_i\, n_j\,. \qquad (1)$$

The first term in Eqn (1) represents the strong on-site FM exchange between the local spin $S = 3/2$ and the spin of conduction electron. This exchange interaction is of the Hund nature, with the local spin $S = 3/2$ being due to the fact that the cubically symmetric crystal field splits the five d orbitals of Mn into three localized t_g orbitals and two delocalized e_g orbitals as shown in Fig. 1. In Eqn (1), the symbol $\langle ij\rangle$ indicates summation over z nearest neighbors.

In real manganites, the Hund-rule interaction J_{H} is on the order of 1 eV.

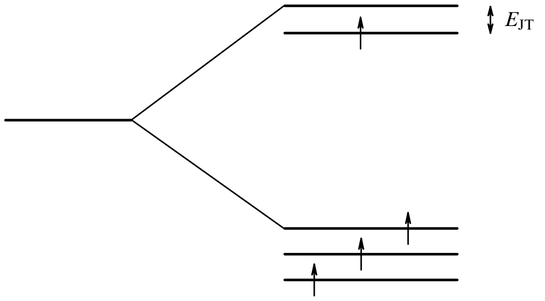

Figure 1. Jahn – Teller Mn^{3+} ion in the octahedral environment.

The second term in Eqn (1) is the kinetic energy of the conduction electrons. The projection operator P corresponds to the case of singly occupied e_g orbitals (a strong one-center Coulomb repulsion prevents two conduction electrons from occupying one and the same site). Note that a strong electron – lattice interaction [24] significantly reduces the effective width W of the conduction band ($W = 2tz$), actually $t \sim 0.3$ eV.

The third term in Eqn (1) is a weak AFM exchange between local spins on neighboring sites, with $J_{ff} \sim 0.01$ eV.

Finally, the last term describes the Coulomb interaction between conduction electrons at neighboring sites. The strength of this interaction is typically $V \sim 0.7$ eV.

Note that although this model assumes the Jahn – Teller gap E_{JT} to be wide and hence neglects the presence of two conduction bands for the e_g electrons, still it is adequate to explain the spin and charge aspects of our problem and to provide a qualitative understanding of the global features of the manganites' phase diagram. The physical aspects related to the orbital ordering in the system are neglected in this discussion [25 – 27].

3. Low-doping case

We now return to the basic model (1) and consider first the low-doping case, i.e., that with low density of itinerant electrons (holes). The Coulomb interaction can then be neglected and the ferromagnetic Kondo lattice model is applicable in its conventional form. We can confine ourselves to the tight-binding case as discussed at the beginning of this section. In this limit, the following chain of inequalities holds

$$J_{\mathrm{H}}S \gg W \gg J_{ff}S^2\,, \qquad (2)$$

and the basic physics of the problem is associated not with the standard Ruderman – Kittel – Kasuya – Yosida (RKKY) interaction but with the so-called double-exchange mechanism [28 – 30]. The ferromagnetic Kondo lattice satisfying inequality (2) is usually called the double-exchange model. Our task here is to construct a phase diagram for this model at $T = 0$, and we will achieve this by first finding the optimum energies of all the homogeneous states possible for the system and then comparing these energies with the energy of the phase-separated state. We will consider the collinear AFM state, canted state, and the collinear FM state as possible homogeneous states. For the phase-separated states, the simplest possible scenario of FM spin polarons (droplets) within the AFM matrix will be analyzed. Before proceeding to a more detailed analysis, we should remind the reader of the physical origin of a canted state in the double-exchange model [28, 30]. In the classical picture, it is known that an electron cannot move among antiferromagnetically aligned spins, and it is therefore favorable for the electron to cant one sublattice relative to the other as it jumps to a neighboring site. The effective hopping integral in a classical canted state is then $t_{\text{eff}} = t\cos(\theta/2)$ and is related to the spinor nature of the electron wave function. The reason is that in the strong Hund coupling limit, $J_{\text{H}} \gg W$, the conduction electron and the local spin together form a coupled state with a total spin $S^{\text{tot}} = (S + 1/2)$. Therefore, if the AFM sublattices are rotated by an angle θ with respect to one another, then the electron's spinor wave function should be rotated by $\theta/2$ as the electron jumps between sites. The canting angle itself then turns out to be a function of the density of conduction electrons. In a classical problem, this angle is found from the condition that the following expression† for the energy of the system be minimized:

$$E = -ztn\cos\frac{\theta}{2} + \frac{1}{2}zJ_{ff}S^2\cos\theta\,, \tag{3}$$

where z is the number of nearest neighbors, and n is the conduction-electron density.

The first term in this equation accounts for the kinetic energy gain related to the arising conduction band, and the second is the loss in the antiferromagnetic interaction energy of local spins. Note that the constant term $J_{\text{H}}S/2$ related to the Hund-rule on-site coupling is omitted in Eqn (3). The same will be done below in any energy expression because this term causes only a constant shift in energy zero and does not affect our analysis. Minimization of the energy (3) with respect to the parameter $\cos(\theta/2)$ yields [30]

$$\cos\frac{\theta}{2} = \frac{tn}{2J_{ff}S^2}\,. \tag{4}$$

Consequently,

$$E = -\frac{zt^2n^2}{4J_{ff}S^2} - zJ_{ff}S^2\,. \tag{5}$$

Thus, in the absence of doping ($n = 0$), we have the canting angle $\theta = \pi$, corresponding to a collinear AFM state. For $n \neq 0$, the canting angle $\theta \neq \pi$, and we are dealing with a canted state. Finally, for $n = n_c = 2J_{ff}S^2/t$, the canting angle $\theta = 0$, implying a transition to a collinear FM state.

A quantum picture of a canted state was analyzed by Nagaev [31]. According to this picture, there are two bands, t_+ and t_-, for the motion of conduction electrons, corresponding to two different projections of the total spin, $S_z^{\text{tot}} = S + 1/2$ and $S_z^{\text{tot}} = S - 1/2$. Apparently, these two bands are naturally in thermodynamic equilibrium, i.e., have a common chemical potential μ. The de Gennes classical description of this situation is obtained by taking the limit $t_- \to 0$.

A quantum treatment shows that for $\theta = \pi$, i.e., in the case of a collinear AFM state, we have $t_+ = t_- = t/\sqrt{2S+1}$. This is where the main difference between the quantum and classical descriptions of spin canting lies. In the quantum picture, the band width t_- for $S \gg 1$ is small only as $1/\sqrt{S}$, unlike the de Gennes limit, where it is small as $1/S$. The classical limit is attained only in the vicinity of a transition to a collinear FM state, i.e., for $\theta \to 0$. In this case, for $S \gg 1$, we have $t_+ = t$ and $t_- = t/(2S+1)$.

Returning again to the low-doping ($n \to 0$) case, we see that the collinear AFM state with an angle $\theta = \pi$ proves to remain energetically favorable up to the critical value of the charge carrier density n_{c1} given by [31, 32]

$$n_{\text{c1}} = \frac{\pi^4}{3}\left[8\,\frac{J_{ff}S^2}{zt}\,\frac{1}{\sqrt{2S+1}}\right]^3. \tag{6}$$

It is easy to see that the onset of the canted state corresponds to the situation where, on the order of magnitude, $n_{\text{c1}} \sim (J_{ff}S^2/t\sqrt{S})^3$, i.e., parametrically is much smaller than the de Gennes estimate $n_{\text{c}} \sim (J_{ff}S^2/t)$ for a transition to a collinear FM state.

This is another manifestation of the significant difference which exists between the classical and quantum approaches to the problem. In the classical treatment, $n_{\text{c1}} \equiv 0$ in the tight-binding large-spin limit (i.e., when $J_{ff}S^2/t \ll 1$, $S \gg 1$), and spin canting occurs for arbitrarily low doping levels. In the quantum case, spin canting occurs only for densities $n > n_{\text{c1}}$. The physical mechanism allowing the electron (hole) hopping in an AFM environment in the quantum case is related to the possibility of coherent string-type motion [33]. This motion occurs as an electron hops from a state with a total spin projection $S_z^{\text{tot}} = S + 1/2$ on one site to a $S_z^{\text{tot}} = S - 1/2$ state on a neighboring site, then hops back to the $|S_z^{\text{tot}} = S + 1/2\rangle$ state, etc., thus leading to the formation of a band of width $2zt/\sqrt{2S+1}$.

At doping levels $n > n_{\text{c1}}$, a two-band quantum canted state arises, but at $n = n_{\text{c2}} \approx (27/2)n_{\text{c1}}$ [34], the second quantum canting band turns out to be empty, $n_- = 0$, $n_+ = n$, indicating a transition from a two-band to a one-band quantum spin canting. At $n \gtrsim n_{\text{c2}}$, the canting angle θ is still close to π and hence the band width t_+ still not much larger than the band width t_- ($t_+ \gtrsim t_-$). The one-band nature of spin canting in this case is due to the fact that at $n > n_{\text{c2}}$ the bottom of the second band lies above the chemical potential level (Fig. 2).

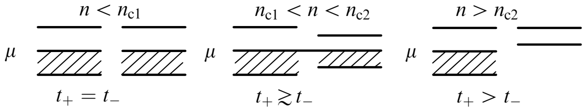

Figure 2. Location of t_+ and t_- bands as a function of doping level (schematic).

The band width t_+ is still determined by the quantum formula

$$t_+ \approx \frac{t}{\sqrt{2S+1}} + \frac{t}{2}\cos\frac{\theta}{2}\,.$$

A transition to a classical one-band spin canting occurs only at much higher densities [34]

$$n = n_{\text{c3}} = \frac{4J_{ff}S^2}{t}\,\frac{1}{\sqrt{2S+1}}\,. \tag{7}$$

At these densities, we have

$$\cos\frac{\theta}{2} \approx \frac{tn_{\text{c3}}}{2J_{ff}S^2} = \frac{2}{\sqrt{2S+1}}\,.$$

---

† **Note from the Editors.** In the English translation some formulas were changed by the authors.

As a result,

$$t_{+} \approx t \cos \frac{\theta}{2}\,; \qquad t_{-} \approx \frac{t}{2S+1}\,,$$

leading to the de Gennes classical canted state.

Finally, at $n > n_{c4} = 2J_{ff} S^2/t$, we have $\theta = 0$, and the classical canted state transforms into a collinear FM state.

To summarize, we arrive at the following picture illustrating the dependence of the optimum energy of the homogeneous state of a system on the density n:

at $0 < n < n_{c1}$, we have a collinear AFM state;

at $n_{c1} < n < n_{c2}$, two-band quantum spin canting arises;

at $n_{c2} < n < n_{c3}$, one-band quantum spin canting takes place;

at $n_{c3} < n < n_{c4}$, the classical canted state of de Gennes occurs; and

at $n > n_{c4}$, a collinear FM state is stabilized.

The energy of the homogeneous state of the system is plotted as a function of density n in Fig. 3.

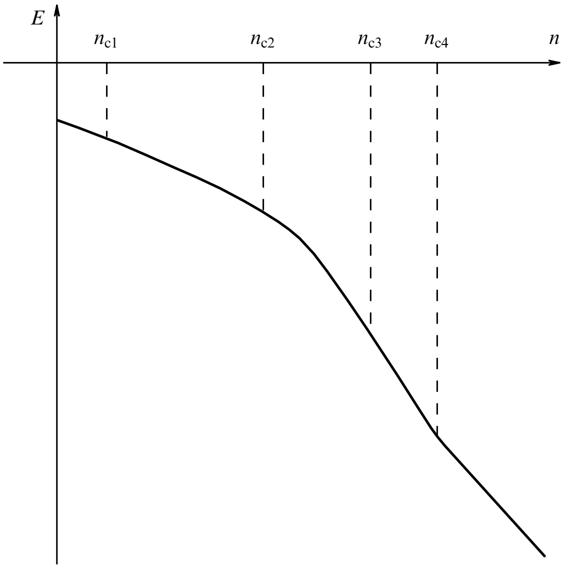

Figure 3. Variation of the energy of the homogeneous state of a system versus density n.

3.1 Stability of the homogeneous state

Now let us check the stability of the solutions we have obtained for the energy of the homogeneous state of the system. To do this, we need to know the sign of the inverse compressibility $\kappa^{-1} = \mathrm{d}^2E/\mathrm{d}n^2$ for all the solutions. It turns out that for $n < n_{c1}$ one has $\mathrm{d}^2E/\mathrm{d}n^2 > 0$ and the collinear AFM state corresponds to at least a local minimum of energy. Similarly, for $n > n_{c4}$ we have $\mathrm{d}^2E/\mathrm{d}n^2 > 0$, and a collinear FM state is at least a local minimum. However, for all densities $n_{c1} < n < n_{c4}$ we have $\mathrm{d}^2E/\mathrm{d}n^2 < 0$, and the canted state is absolutely unstable. The simplest way to see this is to consider the classical de Gennes spin canting, in which taking the second derivative of the energy, Eqn (5), with respect to the density yields

$$\kappa^{-1} = -\frac{zt^2}{2J_{ff} S^2} < 0\,. \tag{8}$$

Of course, in deriving Eqn (8) we have ignored the condition of local charge neutrality as well as the interaction between the electron system and the lattice. But however crude the estimate, formula (8) sends a very disturbing message, leading one to question the stability of a canted state. It is to be emphasized in this connection that the negative sign of compressibility always indicates the instability of a homogeneous state toward phase separation. In the next section, we will consider the simplest case of a phase-separated state, namely the formation of FM polarons within an AFM matrix, and we will show that this state is more favorable energetically than all other homogeneous states over the entire density range of interest here, $0 < n < n_{c4}$. Note also that at $n > n_{c4}$ this state is energetically more favorable than a collinear FM state.

3.2 The energy of a state with ferromagnetic polarons within an antiferromagnetic matrix

The energy of the simplest phase-separated state with FM polarons within an AFM matrix is given by the expression [4, 32]

$$E_{\mathrm{pol}} = -tn\left(z - \frac{\pi^2 a^2}{R^2}\right) + \frac{4}{3}\,\pi\,\frac{J_{ff} z S^2}{2}\left(\frac{R}{a}\right)^3 n - \frac{1}{2}\,J_{ff} z S^2\left[1 - \frac{4}{3}\pi n\left(\frac{R}{a}\right)^3\right], \tag{9}$$

where R is the radius of an FM polaron (ferron), and a is the lattice parameter. Accordingly, $\Omega = (4/3)\pi(R/a)^3$ is the volume of an FM polaron in the three-dimensional isotropic case measured in unit cell volumes. We assume that an FM polaron has a spherical shape in this case. A polaron within an AFM matrix is shown schematically in Fig. 4.

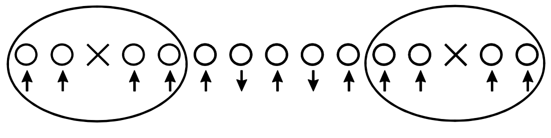

Figure 4. FM polarons with one conduction electron within an insulating AFM matrix. The crosses denote conduction electrons localized at the center of a ferron.

We emphasize that the first term in Eqn (9) describes the kinetic energy gain (an electron in an FM spin environment can be at the bottom of the conduction band). The ta^2/R^2 correction to the term tnz corresponds to the localization energy of an electron in a ferromagnetic droplet of radius R. The second term in Eqn (9) is the loss in the Heisenberg interaction energy between localized spins within the ferromagnetic droplet. Finally, the third term describes the AFM interaction energy between spins in a region free of FM polarons.

Note that at charge-carrier densities

$$n = n_{c5} = \frac{3}{4\pi}\left(\frac{a}{R}\right)^3,$$

FM polarons start overlap, thus bringing the entire sample into an FM state. The optimum polaron radius is obtained from the energy minimization condition $\mathrm{d}E/\mathrm{d}R = 0$. In the three-dimensional isotropic case [15], we have

$$R_{\mathrm{pol}} = a\left(\frac{\pi t}{2zJ_{ff} S^2}\right)^{1/5} \tag{10}$$

and hence

$$n_{c5} = \frac{3}{4\pi}\left(\frac{2zJ_{ff}S^2}{\pi t}\right)^{3/5}.$$

Note that $n_{c5} \sim 0.16$ in real manganites, and consequently $R \sim (2-3)a \sim 10$ Å.

As a result, the optimum energy of an inhomogeneous (polaron) state can be written in the form

$$E_{\mathrm{pol}} = -ztn + \frac{5}{3}\,\pi n(\pi t)^{3/5}(2zJ_{ff}S^2)^{2/5} - \frac{1}{2}\,zJ_{ff}S^2\,. \quad (11)$$

Clearly, both the polaron energy, Eqn (11), and the energy of the de Gennes canted state, Eqn (5), were determined by the variational procedure

$$\frac{\mathrm{d}E_{\mathrm{pol}}}{\mathrm{d}R} = 0\,, \qquad \frac{\mathrm{d}E_{\mathrm{cant}}}{\mathrm{d}\cos(\theta/2)} = 0\,.$$

It is, however, easy to see (Fig. 5) that the polaron state approximates the exact ground state of the system much better than all the optimum energies of homogeneous states do.

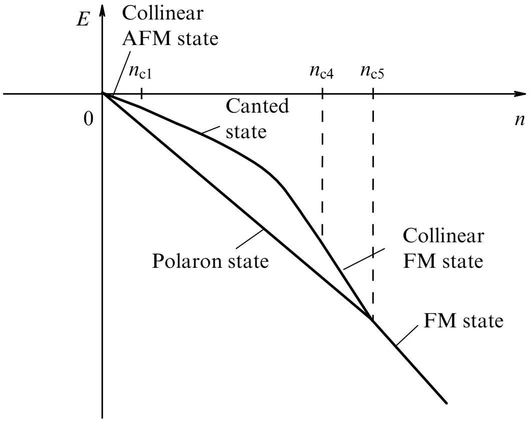

Figure 5. Energies of homogenous and polaron states as functions of the charge-carrier density.

3.3 Electron – hole symmetry of the phase diagram of a ferromagnetic Kondo lattice

The phase diagram of the ferromagnetic Kondo-lattice model with no Coulomb interaction between the electrons exhibits a pronounced re-entrant behavior or, in other words, electron – hole symmetry. Indeed, let us consider now the opposite corner of the phase diagram, one where the electron density $n \to 1$ and hence $\delta = 1 - n \ll 1$. Note that if n is the electron density, then δ is the hole density.

It is seen that for $\delta = 0$, in the limit of a strong on-site Hund exchange, we again obtain an AFM ground state, but now for the spins $S + 1/2$. For low hole doping, $0 < \delta \ll 1$, a few 'unpaired' spins S appear amidst 'paired' $S + 1/2$ spins (Fig. 6).

Furthermore, electron motion between neighboring local spins is in fact equivalent to interchanging an unpaired spin S with a paired spin $S + 1/2$. Thus, for a small number of holes, $\delta \ll 1$, the objects that effectively act as charge carriers are unpaired spins S, the direction of their motion being opposite to that of the holes. This situation is entirely equivalent to that in the $t-J$ model [35]. In our case holes (Zhang – Rice singlets in the $t-J$ model [35]) are presented by the paired spins $S + 1/2$. In HTSCs, the Zhang – Rice singlet is a local Kondo singlet contracted to a magnetic copper site [36]. We wish to emphasize that in our case, a bound state of a local spin plus a conduction electron spin, with a total spin $S + 1/2 = 2$, contracts to a magnetic Mn site. The qualitative arguments above allow us to obtain the expressions we need for the dominating matrix elements for the case of low hole doping, $\delta \ll 1$. In particular, $J_{ff}S^2 \to J_{ff}(S + 1/2)^2$. Accordingly, for the hopping matrix element for the string motion of an unpaired spin S in the AFM medium of $S + 1/2$ spins, the replacement

$$\frac{t}{\sqrt{2S+1}} \to \frac{t}{\sqrt{2(S+1/2)+1}}$$

must be made. At the same time, for the motion of an unpaired spin S in the FM medium of $S + 1/2$ spins, the effective hopping matrix element remains unchanged and is t as before. As a result, also for the opposite corner of the phase diagram ($1 - n = \delta \ll 1$), the global energy minimum will correspond to FM polarons within an AFM matrix of $S + 1/2$ spins. The critical hole density, i.e., one at which polarons start overlapping and the entire sample becomes FM, will then be given by

$$\delta_{c5} = \frac{3}{4\pi}\left(\frac{2zJ_{ff}(S+1/2)^2}{\pi t}\right)^{3/5}. \quad (12)$$

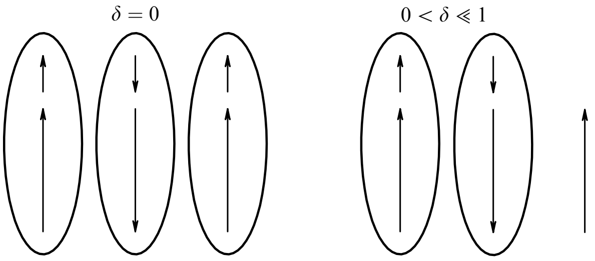

Figure 6. Unpaired spins S in the midst of paired spins $S + 1/2$ for the low hole doping case $0 < \delta \ll 1$.

Finally then, the phase diagram of the ferromagnetic Kondo-lattice model with no Coulomb interaction has the schematic form shown in Fig. 7.

At an electron density $n = 0$, an AFM insulator with spin S is stabilized. For $0 < n < n_{c5}$, FM metal polarons arise within an insulating AFM matrix. For $n_{c5} < n < 1 - \delta_{c5}$, FM metal is stabilized over the entire volume of the sample. At an electron density $1 - \delta_{c5} < n < 1$, the phase diagram of the

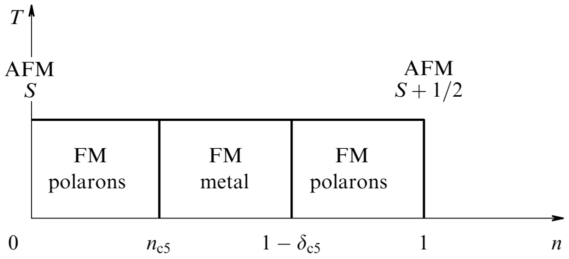

Figure 7. Phase diagram of temperature versus electron density for the ferromagnetic Kondo-lattice model (schematic).

ferromagnetic Kondo-lattice model has a clearly pronounced re-entrant character with FM polarons within an AFM matrix. Finally, for an electron density $n = 1$ we again obtain an AFM insulator, but this time with a sublattice spin $S + 1/2$. Note that in real manganites the phase diagram has a marked asymmetry between electron ($n \ll 1$) and hole ($\delta = 1 - n \ll 1$) doping and is dominated by orbital ordering [21, 23, 25–27]. Along with this strong asymmetry, there are other features in the phase diagram of real manganites which together make it much richer than that of Fig. 7. This is seen particularly clearly in the electron density range $n_{c5} < n < 1 - \delta_{c5}$, where the metallic FM phase is stabilized in the simplest ferromagnetic Kondo model. This richness depends crucially on the Coulomb interaction between electrons, to be considered in detail in the next section.

4. Role of the Coulomb interaction between electrons

We now return to the basic theoretical model (1) and modify the Hamiltonian of the ferromagnetic Kondo lattice by adding the interaction between conduction electrons located at neighboring sites. The discussion of Section 2 shows that we are dealing with the strong interaction, $V > t$, case. More specifically, we have the following chain of inequalities for the basic model (1):

$$J_{\mathrm{H}} S > V > zt > J_{ff} S^2 . \tag{13}$$

We emphasize that the condition $V > t$ actually holds for a dilute Coulomb gas with correlation length $r_s > 1$. Thus, instead of the weak binding case, where perturbation theory and the random phase approximation may be applied, the essentially nonperturbative tight binding case is to be considered. Note that, strictly speaking, $r_s \gtrsim 4$ in manganites, so that in fact both approaches (tight and weak binding) have the right to life. In our view, however, the tight binding approximation should be preferred as it allows all major phenomena encountered in this field to be explained in a simple language at a qualitative level. A characteristic feature of this approach is the occurrence of Wigner crystallization type phenomena. Note that in the limit $V > t$ at electron densities $n \to 1/2$, the charge ordering will appear in the system. Postponing a discussion of this phenomenon, we will here address the low density regime, $n \ll 1$. In this case, the ferromagnetic Kondo-lattice model stabilizes the state with FM polarons within an AFM matrix. For $n \ll n_{c5} = (3/4\pi)(a/R_{\mathrm{pol}})^3$, the polaron radius R_{pol} obeys the inequalities $a/n^{1/3} \gg R_{\mathrm{pol}} \gg a$, implying (Fig. 8) that the mean distance between the conduction electrons far exceeds the polaron radius, which in turn is much larger than the lattice parameter a.

Thus, for FM polarons (ferrons) with one conduction electron per ferron, even the allowance for the strong Coulomb interaction between neighboring electrons does not lead to a charge redistribution. Therefore, upon including the Coulomb interaction, both the energy of the phase-separated state with FM polarons within an AFM matrix and that of a homogeneous state acquire only a Hartree–Fock correction term proportional to $(z/2)Vn^2$, so that the energy difference $E_{\mathrm{pol}} - E_{\mathrm{hom}}$ between the polaron and homogeneous states remains unchanged, and the global minimum for the energy of the system again corresponds to the FM polaron/AFM matrix state. The most important point to reemphasize here is that there is only one conduction electron in each ferron. Here lies the main difference between the small-scale phase separation and the large-scale separation with a large number of conduction electrons per FM cluster (droplet). Note, however, that within the simplest model (1) and in the case of large-scale separation, the electrical charge within an FM droplet may be made rarefied enough to avoid strong increase in the Coulomb interaction energy. This is likely to be a qualitative explanation of the experiments [19, 20, 23] showing FM droplets, 100–1000 Å across, with a large number of conduction electrons. Note also that the analysis of large-scale phase separation probably requires considering the elastic energy of the lattice distortions caused by the formation of an inhomogeneous state. Such distortions may make it easier to change the electron density without violating the electrical neutrality.

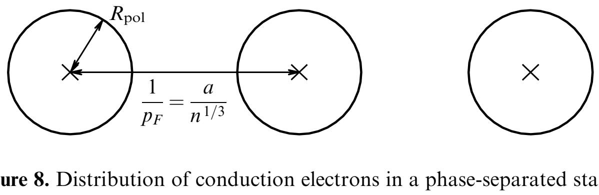

Figure 8. Distribution of conduction electrons in a phase-separated state with FM polarons within an AFM matrix.

4.1 Charge ordering at densities $n \to 1/2$

We consider next the case of large density of conduction electrons, namely that of a quarter-filled band, $n \to 1/2$. At half-filling, $n \to 1$, we know that in the limit of strong on-site repulsion, $U \gg W = 2zt$, so-called Mott–Hubbard localization occurs [37], when all sites are singly occupied and hopping from site to site is not possible because of the strong loss in Coulomb energy. Consider now a situation in which the band width W is so small that not only $U \gg W$, but also $V \gg W$, where V is the Coulomb repulsion between neighboring sites. We address, in other words, the case in which $U \gg V \gg W$. The simplest Hamiltonian for this problem can then be written as

$$\hat{H} = -t \sum_{\langle ij \rangle} P c^{\dagger}_{i\sigma} c_{j\sigma} P + V \sum_{\langle ij \rangle} n_i n_j , \tag{14}$$

where the projection operator again prevents the double occupancy of a lattice site.

Hamiltonian (14) describes two possible localization transitions in the system: in addition to the Mott–Hubbard transition at $n \to 1$, a Verwey localization transition occurs as $n \to 1/2$. This scenario, first proposed to explain a dramatic change in the conductivity of the magnetite $\mathrm{Fe_3O_4}$ (Verwey transition) [38], involves the stabilization of charge-ordered state with a checkerboard arrangement of electrons and holes (Fig. 9).

In this case, hops from one site to another (unoccupied) one are forbidden to an electron because of the high loss in the Coulomb interaction energy of neighboring electrons. Note that if the band width W is even smaller than the Coulomb interaction between electrons located at more distant

Figure 9. Verwey localization scenario for electron densities $n \to 1/2$.

sites ($V \gg V_2 \gg V_3 \gg \ldots \gg V_m \gg W$, where $V_m \sum_i n_i n_{i+m}$ accounts for the Coulomb interaction between electrons a distance ma apart), then varying the carrier density will give rise to a whole cascade of localization phase transitions differing in their ground-state structures. Thus, for $V_2 > W$, the system will exhibit an additional phase transition to a localized state at electron densities $n \to 1/3$.

A more general localization criterion for narrow-band ($a\nabla V(r) > W$) systems was proposed by Kagan and Maksimov [39].

We now return to our simple model, Eqn (14), and first consider the homogeneous state of the system at densities close to $1/2$ for the case $V \gg W$. Note that for a density of $1/2$, charge ordering appears for any value of V, including very low values, the reason being the nesting effect occurring in the simplest model with a constant density of one-electron states. In a more general case, charge ordering at $n = 1/2$ occurs in a threshold manner at $V > V_{\mathrm{cr}}$, where the critical value V_{cr} is on the order of W [40]. A similar result was obtained for the two-orbital model [26].

For an arbitrary electron density $n \neq 1/2$, we will apply to the homogeneous charge-ordered state the same ansatz that was used by Khomskiĭ [40], namely,

$$n_i = n\left[1 + (-1)^i \tau\right] . \tag{15}$$

This expression implies the doubling of the lattice parameter and local densities $n_1 = n(1+\tau)$ and $n_2 = n(1-\tau)$ at neighboring sites. For $\tau \to 1$, this ansatz appears to be quite a natural choice because for $n \to 1/2$ we have $n_1 \to 2n \to 1$ and $n_2 \to 0$ in accord with the simplest checkerboard structure for a charge-ordered state (see Fig. 9). We will later show that in the tight-binding case, $V \gg t$, the value of τ is indeed close to unity. Note that the spectrum of quasiparticles for the charge-ordered state defined by ansatz (15) is given by

$$\varepsilon_{k\pm} = Vnz - \mu \pm \omega_k , \tag{16}$$

where

$$\omega_k = \sqrt{(Vn\tau z)^2 + t_k^2} . \tag{17}$$

Here $t_k = 2t(\cos k_x + \cos k_y + \cos k_z)$ is the spectrum of non-interacting electrons in a cubic lattice, and μ denotes the chemical potential. Note that the quasiparticle spectrum given by Eqns (16), (17) is much like that in a superconductor. Therefore, the first term under the square root in Eqn (17) plays the role of a gap for a charge-ordered state,

$$\varDelta = Vnz\tau . \tag{18}$$

Accordingly,

$$\omega_k = \sqrt{\varDelta^2 + t_k^2} \tag{19}$$

and the only difference from the quasiparticle spectrum of a superconductor,

$$\omega_k = \sqrt{\varDelta^2 + (t_k - \mu)^2} ,$$

is the absence of the chemical potential μ under the square root in Eqn (19).

Thus, the problem of a homogeneous charge-ordered state reduces to that of self-consistently determining the gap $\varDelta$ and the chemical potential μ as functions of density and temperature. More specifically, the values of $\varDelta$ and μ are determined from the set of equations [41]

$$2n = \int \frac{\mathrm{d}^3 k}{\Omega_{\mathrm{BZ}}} \left[f_{\mathrm{F}}(\varepsilon_{k-}) + f_{\mathrm{F}}(\varepsilon_{k+}) \right] ,$$

$$1 = \frac{Vz}{2} \int \frac{\mathrm{d}^3 k}{\Omega_{\mathrm{BZ}}} \frac{1}{\omega_k} \left[f_{\mathrm{F}}(\varepsilon_{k-}) - f_{\mathrm{F}}(\varepsilon_{k+}) \right] , \tag{20}$$

where the $f_{\mathrm{F}}(\varepsilon_{k\pm}) = 1/(\exp\{\varepsilon_{k\pm}/T\} + 1)$ are the Fermi distribution functions, and Ω_{BZ} is the volume of the first Brillouin zone. It is readily seen that the first equation of set (7) is that for the total particle number density, whereas the second is analogous to the self-consistency equation for the superconducting gap in the Bardeen – Cooper – Schrieffer theory. For $T = 0$, we have $f_{\mathrm{F}}(\varepsilon_{k\pm}) = \theta(\varepsilon_{k\pm})$, and the gap $\varDelta$ and the chemical potential μ in fact depend only on the total particle number density n.

Consider the tight-binding case, $V \gg t$. Here for electron densities less than but close to $1/2$ (i.e., for densities $n = 1/2 - \delta$) the set of equations (20) yields

$$\mu(\delta) \approx Vnz(1-\tau) - \frac{4W^2}{Vz}\,\delta^2 \approx \frac{W^2}{3Vz} + \frac{4W^2}{3Vz}\,\delta + O(\delta^2) ,$$

$$\varDelta \approx \frac{Vz}{2}\left[1 - 2\delta - \frac{2W^2}{3V^2 z^2}(1 + 4\delta)\right] . \tag{21}$$

Accordingly,

$$\tau \approx 1 - \frac{2W^2}{3V^2 z^2}(1 + 6\delta) , \tag{22}$$

confirming our assumption that $\tau \to 1$ in the tight-binding limit $V \gg t$. It is important to note that the total energy of the system in a charge-ordered state is given by

$$E_{\mathrm{co}}(\delta) = E_{\mathrm{co}}(0) + \frac{W^2}{3Vz}\,\delta - \frac{2W^2}{3Vz}\,\delta^2 + O(\delta^3) , \tag{23}$$

where $E_{\mathrm{co}}(0) = -W^2/6Vz$ is the energy of the charge-ordered state for quarter-filling, i.e., for the density $n = 1/2$. Note that $|E_{\mathrm{co}}(0)| \ll W$ in the tight-binding limit.

We now proceed to the case of electron densities slightly above $1/2$, i.e., when $n = 1/2 + |\delta|$. In this case, the energy of a charge-ordered state starts to increase rapidly due to the Coulomb interaction contribution, and for each electron added to the system there necessarily exist filled neighboring sites in the checkerboard structure, which increases the total energy of the system by $Vz|\delta|$ at densities $n = 1/2 + |\delta|$. One can say that the upper Verwey band starts filling. As a result, for densities $n = 1/2 + |\delta|$, the total energy of the system becomes

$$E_{\mathrm{co}}(\delta) = E_{\mathrm{co}}(0) + \left(Vz - \frac{W^2}{3Vz}\right)|\delta| - \frac{2W^2}{3Vz}\,\delta^2 + O(\delta^3) . \tag{24}$$

The chemical potential is then

$$\mu = \frac{\mathrm{d}E}{\mathrm{d}n} = Vz - \frac{W^2}{3Vz} - \frac{4W^2}{3Vz}\,|\delta| + O(\delta^2) . \tag{25}$$

It is easily seen that for $\tau \to 1$ the chemical potential experiences a jump by Vz at the point $n = 1/2$. Note that the charge-ordering gap is symmetric at $n > 1/2$ and is given by the formula

$$\Delta \approx \frac{Vz}{2}\left[1 - 2|\delta| - \frac{2W^2}{3V^2z^2}\left(1 + 4|\delta|\right)\right]. \tag{26}$$

As already discussed, the expression for the chemical potential is asymmetric with respect to the transition from densities $n < 1/2$ to $n > 1/2$. This asymmetry, however, is easily removed by shifting all one-electron energy levels and the chemical potential of the system by $Vz/2$, i.e., by defining the quantity $\mu' = \mu - Vz/2$. In terms of μ', Eqns (21) and (25) become

$$\mu' = -\frac{Vz}{2} + \frac{W^2}{3Vz} + \frac{4W^2}{3Vz}\,\delta\,, \qquad n < \frac{1}{2}\,,$$

$$\mu' = \frac{Vz}{2} - \frac{W^2}{3Vz} - \frac{4W^2}{3Vz}\,|\delta|\,, \qquad n > \frac{1}{2}\,.$$

By analogy with the semiconductor situation, exactly at the point $n = 1/2$ the chemical potential $\mu' = 0$ (Fig. 10) lies in the middle of the band gap. For densities $n = 1/2 - 0$, the chemical potential $\mu' = -Vz/2$ coincides with the upper edge of the filled Verwey band.

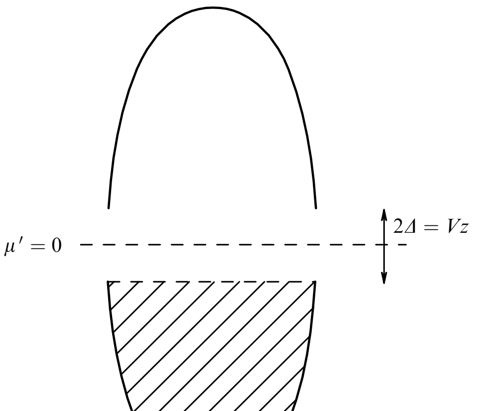

Figure 10. Band structure of the Verwey model for $n = 1/2$. The lower Verwey band is completely filled. The upper Verwey band is empty. The chemical potential $\mu' = 0$ is in the middle of the band gap of width 2Δ.

4.2 Stability of a charge-ordered state at densities close to $n = 1/2$

We now proceed to examine the stability properties of the charge-ordered state. For densities close to $n = 1/2$, the dependence of its energy on the density is as shown in Fig. 11.

From Fig. 11 it can be seen that the charge-ordered state is unstable. Indeed, a calculation of the inverse compressibility $\kappa^{-1} = \mathrm{d}^2E/\mathrm{d}n^2$ using expressions (23), (24) for the energy of the system yields

$$\frac{1}{\kappa} = \frac{\mathrm{d}^2E}{\mathrm{d}n^2} = \frac{\mathrm{d}^2E}{\mathrm{d}\delta^2} = -\frac{4W^2}{3Vz} < 0\,. \tag{27}$$

The negative sign indicates that the system is unstable toward phase separation at $\delta \neq 0$. We wish to emphasize that the presence of a kink (discontinuity in the first derivative) in Fig. 11 related to the rapidly growing linear term $Vz|\delta|$ in the total energy at $n > 1/2$ leads to profound consequences. Indeed, from the global energy and particle number conservation conditions, a state with a density of $n < 1/2$ can only be separated into phases with densities $n_1 < n < 1/2$ and $n_2 = 1/2$. Correspondingly, a state with density $n > 1/2$ can only be separated into phases with densities $1/2 < n < n_1$ and $n_2 = 1/2$. Now consider the case in which the density of the system is exactly $n = 1/2$. From particle number conservation, such a state can be separated only into phases with densities $n_1 < 1/2$ and $n_2 > 1/2$. This separation is energetically unfavorable, however, because of the presence of a rapidly growing linear term in the energy of the second $(n_2 > 1/2)$ phase. Thus, the decay of a state with a density $n \equiv 1/2$ is energetically forbidden and the state is stable in a certain sense. The following section considers the simplest phase-separation scenario for a state with a density $n < 1/2$. We will show that in simple models this scenario corresponds to the formation of metallic droplets of small radius within a charge-ordered matrix.

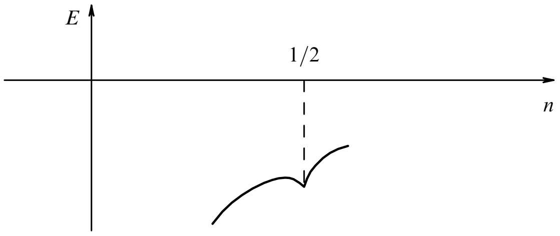

Figure 11. Energy of the charge-ordered state as a function of the density for $n \to 1/2$.

4.3 The simplest example of phase separation in the Verwey model at densities $n < 1/2$

We now return to the model (14) and write down the expression for the energy in the framework of the simplest phase-separation scenario of small-radius metallic droplets in a charge-ordered matrix. This expression has the form [41]

$$E_{\mathrm{drop}} = -t n_{\mathrm{drop}}\left(z - \frac{\pi^2 a^2}{R^2}\right) - \frac{W^2}{6Vz}\left[1 - \frac{4}{3}\,\pi n_{\mathrm{drop}}\left(\frac{R}{a}\right)^3\right], \tag{28}$$

which corresponds to the situation illustrated in Fig. 12 and describes the process in which metallic droplets with one conduction electron are formed in a charge-ordered matrix.

In this expression, as in Eqn (9), R is the radius of the droplet, and a is the interatomic spacing. The first term in Eqn (28) describes the kinetic energy gain due to the localization of an electron within the droplet. The second

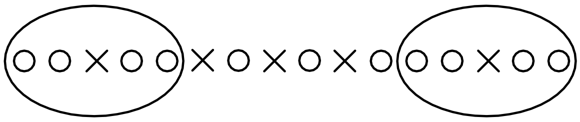

Figure 12. Simplest phase separation scenario involving the formation of metallic droplets with one conduction electron within a charge-ordered matrix.

term is the energy of charge ordering in the insulating region of the sample. The parameter n_{drop} in Eqn (28) is the concentration of metallic droplets. Note that both in Eqn (9) for a magnetic polaron and in Eqn (28) for a metallic droplet, a surface energy term can be incorporated into the total energy of the system. This term, however, is of order W^2R^2/V for a metallic droplet in a charge-ordered matrix, so that for $R \gg a$ it is always small compared to the volume energy term proportional to R^3 and will be neglected in the following discussion. Minimization of the energy (28) with respect to the droplet radius R yields the condition

$$\frac{R}{a} \propto \left(\frac{V}{t}\right)^{1/5} . \tag{29}$$

As a result, at the critical droplet concentration

$$n_{\text{drop cr}} = \frac{3}{4\pi}\left(\frac{a}{R}\right)^3 \propto \left(\frac{t}{V}\right)^{3/5} \tag{30}$$

the metallic droplets overlap and the entire sample undergoes a transition to a metallic state. Expression (30) is in fact the analogue of the Nagaoka theorem for the Verwey model (14). Note that, when using Eqn (30) for the critical droplet concentration, the total energy of the system (28) can be rewritten as

$$E_{\text{drop}} = -tn_{\text{drop}}\left(z - \alpha n_{\text{drop cr}}^{2/3}\right) - \frac{W^2}{6Vz}\left[1 - \frac{n_{\text{drop}}}{n_{\text{drop cr}}}\right], \tag{31}$$

where α is a numerical coefficient of order unity.

Note that the ratio $n_{\text{drop}}/n_{\text{drop cr}}$ in Eqn (31) describes the relative volume $\Omega_{\text{drop}}/\Omega$ occupied by droplets. This volume can be found from the condition for the conservation of the total number of particles in the system, which reads

$$N = \frac{1}{2}(\Omega - \Omega_{\text{drop}}) + n_{\text{drop cr}}\Omega_{\text{drop}} = n\Omega , \tag{32}$$

where n is the average density of conduction electrons.

From condition (32), the required relation follows immediately as [41]

$$\frac{\Omega_{\text{drop}}}{\Omega} = \frac{1/2 - n}{1/2 - n_{\text{drop cr}}} . \tag{33}$$

The droplet concentration in Eqn (31) is then

$$n_{\text{drop}} = n_{\text{drop cr}}\frac{1/2 - n}{1/2 - n_{\text{drop cr}}} = n_{\text{drop cr}}\frac{\delta}{\delta_{\text{cr}}} , \tag{34}$$

where again, as in the homogeneous state, $\delta = 1/2 - n$ is the deviation of the density from $1/2$. From Eqn (32) it follows that $n_{\text{drop}} = 0$ at $n = 1/2$. Accordingly, at the density $n_{\text{drop}} = n_{\text{drop cr}}$ we have $\delta = \delta_{\text{cr}} = 1/2 - n_{\text{drop cr}}$. Finally, the energy of the phase-separated state is

$$\begin{aligned} E_{\text{drop}} &= -t\frac{\delta}{\delta_{\text{cr}}}n_{\text{drop cr}}\left[z - \alpha n_{\text{drop cr}}^{2/3}\right] - \frac{W^2}{6Vz}\left(1 - \frac{\delta}{\delta_{\text{cr}}}\right) \\ &\approx -\frac{W}{2}\frac{\delta}{\delta_{\text{cr}}}n_{\text{drop cr}} - \frac{W^2}{6Vz}\left(1 - \frac{\delta}{\delta_{\text{cr}}}\right) . \end{aligned} \tag{35}$$

Comparison of the energy (35) with the energy (23) of the charge-ordered state shows that we have, for densities $n_{\text{drop cr}} < n < 1/2$,

$$E_{\text{drop}} - E_{\text{co}} \approx -\frac{W}{2}\frac{\delta}{\delta_{\text{cr}}}n_{\text{drop cr}} < 0 .$$

Thus, a phase-separated state with small metallic droplets is more favorable than a homogeneous state. Note that a phase-separated state with small metallic droplets within a charge-ordered matrix is also more favorable than the complete separation into two large clusters, one metallic and the other charge-ordered (Fig. 13).

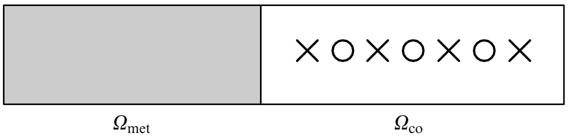

Figure 13. Complete phase separation into two large clusters (metallic and charge-ordered).

Indeed, the energy of a fully separated state is given by

$$E_{\text{tot sep}} = E_{\text{met}}\frac{\Omega_{\text{met}}}{\Omega} + E_{\text{co}}\frac{\Omega_{\text{co}}}{\Omega} , \tag{36}$$

where $\Omega_{\text{met}}/\Omega$ and $\Omega_{\text{co}}/\Omega$ are the relative volumes occupied by the metallic and charge-ordered clusters,

$$E_{\text{met}} = -tzn_{\text{met}} + \beta tn_{\text{met}}^{5/3} + \frac{z}{2}Vn_{\text{met}}^2 \tag{37}$$

is the energy density in the metallic cluster, and

$$E_{\text{co}} = -\frac{W^2}{6Vz}$$

is the energy density in the charge-ordered cluster.

Minimization of the energy density (37) with respect to n_{met} now yields for the metallic cluster

$$\begin{aligned} n_{\text{met}\,0} &\approx \frac{t}{V} , \\ E_{\text{met}} &\approx -\frac{t^2z}{2V} = -\frac{W^2}{8Vz} . \end{aligned} \tag{38}$$

As a result, for densities $n_{\text{met}\,0} < n < 1/2$, the system separates fully into a metallic phase with density $n_{\text{met}\,0}$ and a charge-ordered phase with density $1/2$. By analogy with Eqn (32), the relative volumes of the phases are given by

$$\frac{\Omega_{\text{met}}}{\Omega} = 1 - \frac{\Omega_{\text{co}}}{\Omega} = \frac{1/2 - n}{1/2 - n_{\text{met}\,0}} = \frac{\delta}{\delta_0} . \tag{39}$$

Accordingly, the energy of the fully separated state takes the form

$$E_{\text{tot sep}} \approx -\frac{W^2}{8Vz}\frac{\delta}{\delta_0} - \frac{W^2}{6Vz}\left(1 - \frac{\delta}{\delta_0}\right) . \tag{40}$$

It is readily seen that, by analogy with the Nagaoka theorem for the Hubbard model, the density of a metallic cluster is $n_{\text{met}\,0} < n_{\text{drop cr}}$ in the Verwey model, and hence $E_{\text{drop}} < E_{\text{tot sep}}$. Physically, this is related to the fact that even when metallic droplets overlap, each conduction electron is within a sphere of radius $R/a \sim (V/t)^{1/5}$ and thus is effectively farther from other electrons than it would be in the case of full phase separation. Therefore, at full phase separation the energy of Coulomb interaction between electrons turns out to be higher than for metallic droplets of small radius.

Note that along with one-electron metallic droplets, a small-scale phase-separation scenario of the kind shown in Fig. 14 can be organized, in which a metallic droplet is formed by replacing one electron with a hole at the center of a droplet.

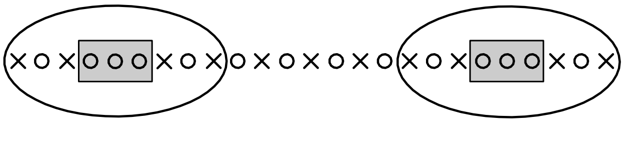

Figure 14. Small-scale phase-separation scenario with an undermelted charge-ordered state within a metallic droplet.

Note, however, that the energy of such an undermelted charge-ordered state ('a resonance-valence bond state' for the Verwey model) is much more difficult to calculate than that for a one-electron metallic droplet, and this problem will not be considered in this review.

In conclusion, we can summarize the main results of this section as follows.

For $V \gg W$ and densities $(t/V)^{3/5} < n < 1/2$, the Verwey model (14) is unstable toward phase separation, and in the simplest case the most energetically favorable phase-separation scenario is that involving small metallic droplets with one conduction electron within a charge-ordered matrix.

Let us now return to the basic model of the ferromagnetic Kondo lattice with a Coulomb interaction, Eqn (1), and determine for it the structure of a phase-separated state for densities close to 1/2.

4.4 Phase separation in the basic model of the ferromagnetic Kondo lattice with a Coulomb interaction for densities close to $n = 1/2$

The energy of a phase-separated state in the basic model (1) for densities close to 1/2 has the form

$$E_{\text{drop}} = -tn_{\text{drop}}\left(z - \frac{\pi^2 a^2}{R^2}\right) + \frac{zJ_{ff}S^2}{2}\,\frac{4}{3}\,\pi\left(\frac{R}{a}\right)^3 n_{\text{drop}} - \frac{1}{2}\,zJ_{ff}S^2\left[1 - \frac{4}{3}\,\pi\left(\frac{R}{a}\right)^3 n_{\text{drop}}\right] - \frac{W^2}{6Vz}\left[1 - \frac{4}{3}\,\pi\left(\frac{R}{a}\right)^3 n_{\text{drop}}\right]. \tag{41}$$

The first three terms in Eqn (41) are in fact identical to the magnetic polaron energy in the double-exchange model (9) but with the electron density n replaced by the droplet density n_{drop}. At the same time, the last term in Eqn (41) is identical to the second term of (28) corresponding to the energy of a homogeneous charge-ordered Verwey state. These coincidences are not surprising, because the basic model (1) is obtained from the double-exchange model by adding the Coulomb term. Minimization of the droplet energy, Eqn (41), with respect to radius R yields [41]

$$\frac{R}{a} \sim \frac{1}{(t/V + J_{ff}S^2/t)^{1/5}}\,. \tag{42}$$

Note that for $t/V \ll J_{ff}S^2/t$, we obtain $R/a \sim (t/(J_{ff}S^2))^{1/5}$), and the double-exchange result (10) is reproduced for the metallic-droplet radius. In the opposite limit $t/V \gg J_{ff}S^2/t$, we have $R/a \sim (V/t)^{1/5}$, and we arrive at the Verwey model result (30). Accordingly, the critical concentration for the overlap of metallic droplets is

$$n_{\text{drop cr}} \sim \left(\frac{t}{V} + \frac{J_{ff}S^2}{t}\right)^{3/5}. \tag{43}$$

Naturally, the droplet concentration in the energy expression (41) for the phase-separated state is again given by

$$n_{\text{drop}} = n_{\text{drop cr}}\,\frac{\delta}{\delta_{\text{cr}}}$$

with $n_{\text{drop cr}}$ from Eqn (43). Physically, minimization of the total energy (41) with respect to the droplet radius implies that there is only one conduction electron inside a metallic droplet and that this electron is surrounded by ferromagnetically ordered local spins. At the same time, outside the droplets, we have a charge-ordered (checkerboard) arrangement of conduction electrons surrounded by antiferromagnetically ordered local spins (Fig. 15).

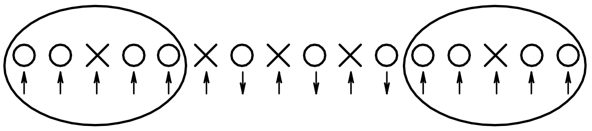

Figure 15. Formation of metallic FM droplets of small radius within a charge-ordered AFM matrix.

This last result illustrates the main difference between the phase-separated states that are obtained in the basic model (1) at densities $n \to 0$ and $n \to 1/2$. At low densities ($n \ll 1$), the conduction electron density outside FM polarons is zero and the entire electrical charge is contained within metallic droplets. At the same time, at densities close to 1/2, most conduction electrons are localized in charge-ordered regions outside the metallic droplets.

Finally, the phase diagram of the model of a ferromagnetic Kondo lattice with a Coulomb interaction includes the following regimes:

(1) For $0 < n < (J_{ff}S^2/t)^{3/5}$, the system separates into metallic FM droplets within an AFM insulating matrix.

(2) For $(J_{ff}S^2/t)^{3/5} < n < (t/V + J_{ff}S^2/t)^{3/5} < 1/2$, the system is an FM metal. Of course, we must have a certain 'window' of parameters to satisfy the inequality on the right-hand side of this expression. As discussed in Section 2, in real manganites we have $t/V \sim 1/2 - 1/3$ and $J_{ff}S^2/t \sim 0.1$. Therefore, the inequality

$$n < \left(\frac{t}{V} + \frac{J_{ff}S^2}{t}\right)^{3/5} < 1/2$$

is not necessarily met. Experimental evidence indicates that the desired parameter range exists for $La_{1-x}Ca_xMnO_3$, but definitely not for $Pr_{1-x}Ca_xMnO_3$.

(3) Finally, for $(t/V + J_{ff}S^2/t)^{3/5} < n < 1/2$, phase separation into metallic FM droplets within an AFM charge-ordered matrix occurs. It is to be emphasized that an ideal AFM structure can only be formed by local spins S. The

large Hund-rule exchange between a local spin S and a conduction electron spin leads to ferrimagnetism in a charge-ordered matrix. Note that for $n \geqslant 1/2$ the phase diagram of the basic model (1) has a qualitatively the same features. At $n = 1/2$ a homogeneous charge-ordered state is stabilized. For $n > 1/2$, metallic FM droplets first appear within a charge-ordered AFM matrix. Qualitatively, the only difference is that, instead of one electron, one hole will now be localized inside the droplet (Fig. 16).

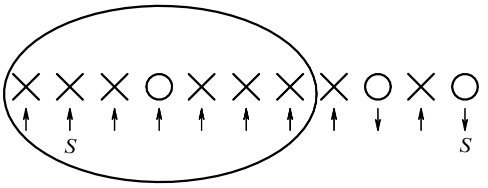

Figure 16. Metallic FM droplet against the background of a charge-ordered AFM structure at densities $n > 1/2$.

As a result of the strong Hund exchange, the phase separation diagram of Fig. 16 becomes equivalent to that shown in Fig. 17.

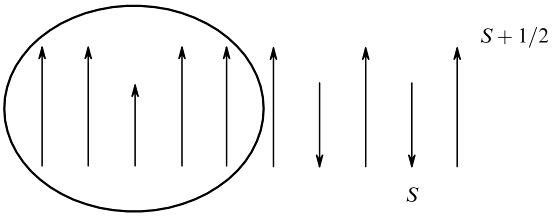

Figure 17. Effective phase-separation diagram at densities $n \gtrsim 1/2$.

In this latter diagram, the effective charge carrier is an unpaired spin S localized at the center of a metallic droplet against the background of ferromagnetically ordered spins $S + 1/2$. Accordingly, outside metallic droplets a ferrimagnetic structure with two antiparallel sublattices of spins $S + 1/2$ and S occurs.

At higher densities, a hole FM metal, or in other words a metallic system of unpaired spins S, appears. At still higher densities $n \to 1$, when $\delta = 1 - n \ll 1$, FM droplets, with unpaired spins S as carriers, appear within an insulating AFM matrix of effective spins $S + 1/2$. The structure of this state is depicted in Fig. 18 and has already been discussed in Section 3 of this review.

Finally, at $n = 1$ ($\delta = 0$), the whole of the sample will be an antiferromagnet with spin $S + 1/2$.

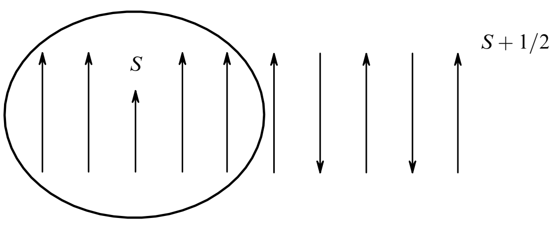

Figure 18. Structure of a phase-separated state at the conduction electron density $n \to 1$.

The phase diagram discussed above is in good qualitative agreement both with experiments on small-scale phase separation in manganites [42–47] and with numerical calculations by Dagotto et al. [48]. Note that real manganites are usually hole-doped, so that experimentally n often means the hole concentration. This does not matter much, however, because of the re-entrant character of the phase diagram for the basic model (1). Nevertheless, the phase diagram of a real manganite differs considerably depending on whether it is electron- or hole-doped. The mechanisms of this asymmetry are not yet completely understood. In particular, the asymmetry can be related to the specificity of orbital ordering in manganites and on the possible formation, as we have mentioned above, of inhomogeneous states other than the droplet structures discussed here, charge- and orbital-ordered stripes, for example. To include all these aspects, however, a theory that goes beyond the model (1) is needed.

Turning now to the experimental confirmation of our results, the beautiful nuclear magnetic resonance experiments on $La_{1-x}Ca_xMnO_3$ [42] should be mentioned first. These experiments, which employed ^{55}Mn nuclei, provided evidence for the existence of two NMR frequencies in a sample (instead of only one as is typical for a homogeneous state), whose frequencies are naturally attributed to the ferromagnetic and antiferromagnetic domains resulting from the phase separation in manganites. NMR measurements at La nuclei in La–Pr manganites led to similar conclusions [43].

Further experimental confirmation of phase separation in manganites comes from recent neutron scattering experiments [44, 47]. They showed that in the case of inelastic scattering there are two spin-wave modes, one of which has quadratic dispersion and corresponds to FM magnons, whereas the other has linear dispersion and corresponds to magnons in the AFM phase.

Note that in elastic neutron scattering experiments the peak intensity $I(q)$ has a Lorentzian shape. The half-width of the peak at low densities $n \sim 0.05$ corresponds to the characteristic polaron radius $R_{\text{pol}} \sim 1/q_0 \sim 10$ Å [44]. At densities n close to 1/2, the line half-width again corresponds to small-scale phase separation with a characteristic polaron size $R_{\text{pol}} \sim 10-20$ Å.

Note that similar measurements of the spin wave spectrum in a magnetic field using the antiferromagnetic resonance technique are interpreted in Ref. [49] as favoring some nontrivial compromise between magnetic polaron formation and homogeneous spin canting. The possibility of such a compromise, first noted by de Gennes in his classical paper [30], relates to a certain amount of inhomogeneous spin canting against the FM background within a magnetic polaron and to a certain amount of inhomogeneous spin canting against the FM background outside the magnetic polaron. Such a structure can in principle be achieved if the ferron wave function decays exponentially, rather than according to a power law, as the distance increases.

Quite recently, further experimental evidence in favor of the polaron picture was obtained by Babushkina et al. [45], who discovered a strongly nonlinear current–voltage characteristic in La–Pr manganites close to the phase boundary between the ferromagnetic and charge-ordered states. This provides indirect evidence for percolative charge transfer [50] naturally activated by the phase separation process. The critical density for the overlap of polarons actually appears as the percolation threshold in this picture [50].

Finally, the experiments of Voloshin et al. [46] showed a shifted magnetization hysteresis in manganites, with the center of the hysteresis loop shifting from the magnetic field $H = 0$ to $H \sim 4-6$ T in the low-density regime. The shift appears quite naturally within the polaron picture. To see this, note that in a magnetic field the effective Heisenberg exchange is

$$J_{ff}^{\text{eff}} S^2 = J_{ff} S^2 - g\mu_{\text{B}} HS\,,$$

where g is the gyromagnetic ratio, and μ_{B} is the Bohr magneton. Therefore, the polaron radius $R/a \sim (t/J_{ff}^{\text{eff}} S^2)^{1/5}$ increases, with the result that in strong magnetic fields polarons start overlapping at lower densities: $n_{\text{cr}}(H) < n_{\text{cr}}(0) = 0.16$.

Note that, recently, more direct experiments supporting the phase separation scenario have been carried out [19, 51]. In Ref. [51], metallic regions inside the insulating matrix were visualized via scanning tunneling microscopy, and in Ref. [19] electron-diffraction and dark-field microscopy showed the existence of metallic domains against the background of a charge-ordered matrix. However, both Ref. [51] and [19] actually report large-scale phase separation, with metallic domains measuring $L \sim 100-200$ Å in size. Thus, the experiments reported in Refs [19] and [51] neither contradict nor decisively verify the polaron picture.

Note also that a phase diagram containing two types of separation and similar to that discussed in this section was predicted in Refs [52, 53] in the analysis of spontaneous ferromagnetism in doped exciton insulators.

4.5 'Temperature' ferrons

In concluding this section, we turn our discussion to yet another kind of inhomogeneous state predicted by the basic model (1) — self-trapped states of conduction electrons of the FM-droplet type (small-radius FM fluctuations) in a ferromagnet near the Curie point. Note that at $T > T_{\text{C}}$, for this concentration range ($n \sim 0.2-0.4$), a transition from the metallic FM phase to the paramagnetic insulator region occurs. This possibility was widely discussed as long ago as in the 1970s (see, for example, Refs [15, 16]), and at present there is direct evidence for this effect from neutron scattering experiments on manganites.

Indeed, by analogy with Eqn (9), above the Curie temperature T_{C} the change in the free energy ΔF due to the formation of ferromagnetic droplets can be written in the form

$$\Delta F = -tn\left(z - \frac{\pi^2 a^2}{R^2}\right) + \frac{4}{3}\,\pi T\left(\frac{R}{a}\right)^3 n \ln(2S+1)\,. \qquad (44)$$

Here the first and second terms represent, respectively, the changes in the energy and entropy of the system due to the formation of FM droplets. We assume that $J_{ff} S^2 \lesssim T_{\text{C}} < T < t$, and that the density n at low temperatures corresponds to the region of existence of the ferromagnetic phase.

Minimization of Eqn (44) with respect to R yields the following estimate for the radius of 'temperature' ferrons:

$$R \sim a\left(\frac{t}{T \ln(2S+1)}\right)^{1/5}. \qquad (45)$$

Thus, we have arrived at a formula of the type (10), with $J_{ff} S^2$ replaced by $T \ln(2S+1)$. Note that such 'temperature' ferrons can significantly affect the magnetic and transport properties of manganites near the Curie point.

5. Phase separation in layered manganites

In the previous sections, we have been mainly concerned with $La_{1-x}Ca_xMnO_3$, $La_{1-x}Sr_xMnO_3$, and $La_{1-x}Ba_xMnO_3$ manganites that have a cubic perovskite structure. Along with these, layered manganites with a $(La, Sr)_{n+1}Mn_nO_{3n+1}$ structure, commonly known as Ruddelsden – Popper phases, are currently attracting great attention. The best known of them are La_2MnO_4, the analogue of the basic HTSC compound La_2CuO_4 ($n = 1$), and the bilayer compound $La_3Mn_2O_7$ ($n = 2$). Note that for $n \to \infty$ we again obtain $La_{1-x}Sr_xMnO_3$, i.e., a normal cubic perovskite.

In the absence of doping and at low concentrations of Sr, layered manganites usually exhibit the so-called A structure (Fig. 19), in which spins in the conducting MnO layer are aligned ferromagnetically but the ferromagnetic moments of neighboring layers are antiparallel to one another. On doping, the physics of layered manganites is similar to that of HTSC compounds.

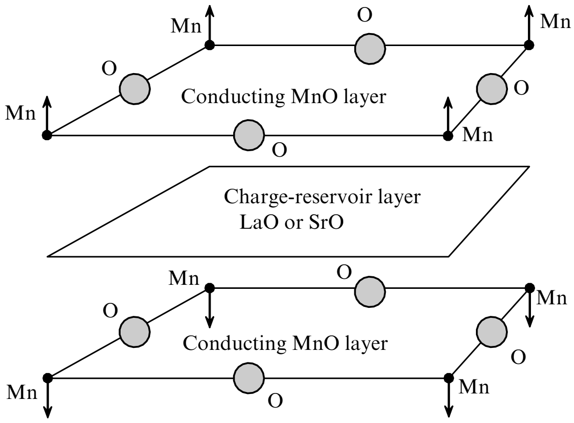

Figure 19. Spin and charge arrangement in layered manganites.

Indeed, all the major magnetic and transport properties of layered manganites are determined by the two-dimensional metallic layers of LaO or SrO, the latter serving the same charge-reservoir role as in HTSCs. At low doping levels the properties of layered manganites are adequately described by the anisotropic double-exchange model. The Hamiltonian of this model is

$$\hat{H} = -J_{\text{H}} \sum_{ia} \mathbf{S}_{ia} \boldsymbol{\sigma}_{ia} - t_{\parallel} \sum_{\langle ij \rangle a\sigma} c_{ia\sigma}^{\dagger} c_{ja\sigma} - t_{\perp} \sum_{ia\sigma} c_{ia\sigma}^{\dagger} c_{ia+1,\sigma}$$
$$- J_{\text{FM}} \sum_{\langle ij \rangle a} \mathbf{S}_{ia} \mathbf{S}_{ja} + J_{ff} \sum_{ia} \mathbf{S}_{ia} \mathbf{S}_{ia+1}\,, \qquad (46)$$

where a denotes the number of a layer, and i and j refer to a lattice site within the layer, the summation running over the neighboring sites. Accordingly, $t_{\parallel}$ and $t_{\perp}$ denote the hopping integrals in and normal to a layer, respectively. Finally, J_{FM} accounts for the FM exchange between local spins inside a layer, and J_{ff} describes the AFM exchange between local spins in neighboring layers. We again consider the case of a large spin, $S \gg 1$, and work in the tight-binding limit, in which the chain of inequalities

$$J_{\mathrm{H}}S \gg \{t_{\parallel}; t_{\perp}\} \gg \{J_{ff}S^2; J_{\mathrm{FM}}S^2\}$$

holds.

In the following sections, we consider the homogeneous canted state and phase separation in layered manganites. Some of the results presented below were obtained by Nagaev [54], the notable exception being the case of ellipsoidal ferrons which he did not consider.

5.1 A canted state in layered manganites

In this case, a conduction electron traveling parallel to the layer must be at the bottom of the conduction band. At the same time its motion perpendicular to the layers must be the one-dimensional analogue of de Gennes' classical spin canting picture. It is therefore reasonable to assume that the spectrum of conduction electrons in the layered case is of the form

$$\varepsilon = -4t_{\parallel} - 2t_{\perp}\cos\frac{\theta}{2}\,, \tag{47}$$

where θ is the canting angle between the FM moments of neighboring metallic MnO layers, and $z = 4$ is the number of the nearest neighbors in a MnO layer on a square lattice. The exact solution of Nagaev's [32] equations for the layered case confirms our assumption. The electron spectrum described by Eqn (47), as in the isotropic case, corresponds to the total site spin $S^{\mathrm{tot}} = S + 1/2$, and to the total spin projection $S_z^{\mathrm{tot}} = S + 1/2$. At the same time, unlike the isotropic situation, the second conduction band, which corresponds to the total spin projection $S_z^{\mathrm{tot}} = S - 1/2$, has the spectrum

$$\varepsilon_{-} = -\frac{4t_{\parallel} - 2t_{\perp}\cos(\theta/2)}{2S+1}\,. \tag{48}$$

Thus, in the layered case the electron spectrum corresponding to the second band contains a small parameter $\varepsilon_{-} \sim 1/(2S+1)$ (cf. Section 3 of the present review). As a result, whatever the level of doping, one can ignore the second band and consider de Gennes' purely classical spin canting picture. Thus, in the layered case there is no such thing as the first critical concentration n_{c1} (see Section 3), and a canted state arises even at densities $n \to 0$. Minimization of the classical canting energy with respect to the parameter $\cos(\theta/2)$ leads to the following layered-case result:

$$\cos\frac{\theta}{2} = \frac{t_{\perp}n}{2J_{ff}S^2}\,. \tag{49}$$

At the critical concentration $n_{\mathrm{c2}} = 2J_{ff}S^2/t_{\perp}$, the canting angle is $\theta = 0$, and the system undergoes a transition to a collinear FM state.

However, a stability analysis of the optimum spin canting energy once again leads to a negative compressibility. Therefore, the conclusion about the instability of a homogeneous canted state toward phase separation also applies to the layered case. To the global minimum of energy there again corresponds phase separation to small-radius FM polarons within an AFM matrix. Let us determine the size and structure of a polaron in this case.

5.2 Magnetic polarons in layered manganites

(a) Consider, first, magnetic polarons of ellipsoidal shape [55]. Analogous to the isotropic case, the energy of a magnetic polaron can be written as

$$E_{\mathrm{pol}} = E_0 - 4t_{\parallel}n - t_{\perp}n\left(2 - \frac{a^2\pi^2}{R_{\perp}^2}\right) + 2J_{ff}S^2n\Omega\,, \tag{50}$$

where Ω is the volume of the FM polaron, $R_{\perp}$ is the polaron radius in the direction perpendicular to the layers, and E_0 is defined by

$$E_0 = -J_{ff}S^2 - 2J_{\mathrm{FM}}S^2\,. \tag{51}$$

Note that the volume of an ellipsoidal magnetic polaron (Fig. 20) is

$$\Omega_{\mathrm{ell}} = \frac{4}{3}\pi\frac{R_{\perp}R_{\parallel}^2}{a^3}\,.$$

Furthermore, in the anisotropic double-exchange model, we have

$$R_{\parallel} = R_{\perp}\sqrt{\frac{t_{\parallel}}{t_{\perp}}} > R_{\perp}\,.$$

This result is consistent with neutron scattering experiments on layered manganites [44]. Thus, the expression for the volume of a polaron can be rewritten as

$$\Omega_{\mathrm{ell}} = \frac{4}{3}\pi\left(\frac{R_{\perp}}{a}\right)^3\frac{t_{\parallel}}{t_{\perp}}\,.$$

Minimizing the magnetic polaron energy (50) with respect to the free parameter $R_{\perp}$ gives

$$R_{\perp} = a\left(\frac{\pi t_{\perp}^2}{4J_{ff}S^2t_{\parallel}}\right)^{1/5}. \tag{52}$$

Consequently, the optimum volume of a magnetic polaron of ellipsoidal shape is

$$\Omega_{\mathrm{ell}} = \frac{4}{3}\pi\left(\frac{\pi t_{\perp}^2}{4J_{ff}S^2t_{\parallel}}\right)^{3/5}\frac{t_{\parallel}}{t_{\perp}}\,. \tag{53}$$

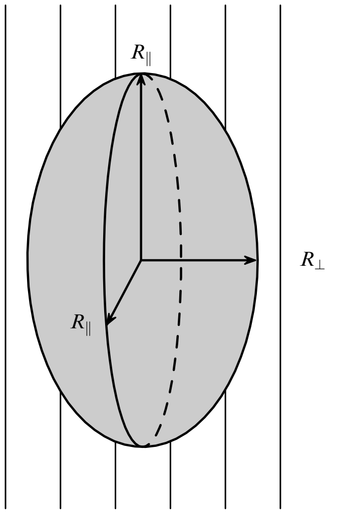

Figure 20. Magnetic polaron of ellipsoidal shape in layered manganites.

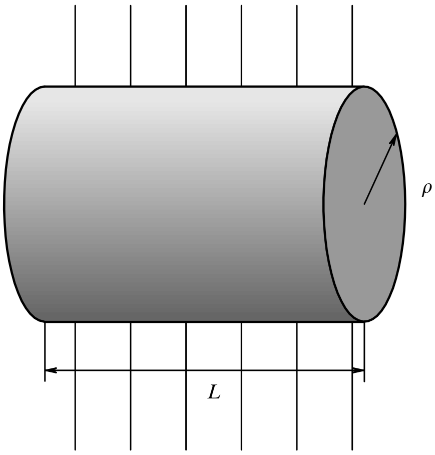

Figure 21. Magnetic polaron of cylindrical shape in layered manganites.

(b) We now proceed to magnetic polarons of cylindrical shape (Fig. 21).

The volume of a cylindrical polaron is

$$\Omega_{\mathrm{cyl}} = \frac{\pi \rho^2 L}{a^3}\,, \tag{54}$$

and its energy is, accordingly,

$$E_{\mathrm{pol}} = E_0 - t_{\parallel} n \left(4 - \frac{9\pi^2 a^2}{16\rho^2}\right) - t_{\perp} n \left(2 - \frac{a^2 \pi^2}{L^2}\right) + 2 J_{ff} S^2 n \Omega\,. \tag{55}$$

Note here that the coefficient $9\pi^2/16$ in the expression for the shift in energy from the band bottom, $-4t_{\parallel}n$, is determined by a zero of the Bessel function: $J_0(x) = 0$ for $x \approx 3\pi/4$. Simultaneously minimizing the polaron energy with respect to L and ρ yields

$$\rho \approx 0.53 L \sqrt{\frac{t_{\parallel}}{t_{\perp}}}\,, \qquad L \approx 0.98 a \left(\frac{4\pi t_{\perp}^2}{t_{\parallel} J_{ff} S^2}\right)^{1/5}. \tag{56}$$

As a result, the optimum volume of a cylindrical polaron is

$$\Omega_{\mathrm{cyl}} \approx \pi\,\frac{L^3}{a^3}\,\frac{t_{\parallel}}{4t_{\perp}} \approx 0.26\pi \left(\frac{4\pi t_{\perp}^2}{J_{ff} S^2 t_{\parallel}}\right)^{3/5} \frac{t_{\parallel}}{t_{\perp}}\,. \tag{57}$$

A direct comparison of the optimum energies for the ellipsoidal and cylindrical cases shows that

$$\frac{E_{\mathrm{ell\,pol}} - \tilde{E}_0}{E_{\mathrm{cyl\,pol}} - \tilde{E}_0} \approx \frac{\Omega_{\mathrm{ell}}}{\Omega_{\mathrm{cyl}}} \approx 0.96\,, \tag{58}$$

where $\tilde{E}_0 = E_0 - 4t_{\parallel}n - 2t_{\perp}n$.

The conclusion is that the ellipsoid is the optimum polaron shape. This is quite reasonable physically because the optimum shape of a polaron (its 'ground state' in a manner) mimics the shape which the electronic spectrum has in the layered case, i.e., $\varepsilon(p) \sim t_{\parallel} p_{\parallel}^2 + t_{\perp} p_{\perp}^2$. Note that in the layered case polarons start overlapping at the critical concentration

$$n_{\mathrm{c}5} = \frac{1}{\Omega_{\mathrm{ell}}} = \frac{3}{4\pi} \left(\frac{4 J_{ff} S^2 t_{\parallel}}{\pi t_{\perp}^2}\right)^{3/5} \frac{t_{\perp}}{t_{\parallel}}\,. \tag{59}$$

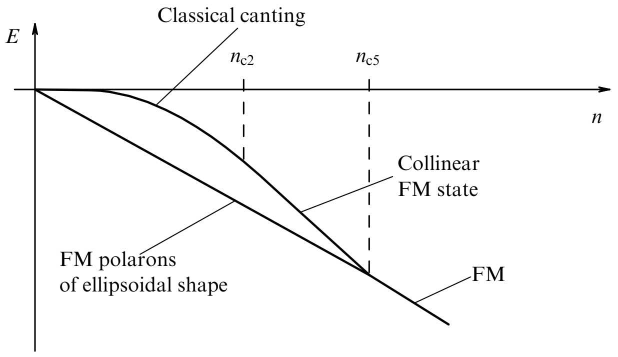

Figure 22. Energy of the system as a function of density in layered manganites.

Note also that for all densities in the range $0 < n < n_{\mathrm{c}5}$, the energy of a polaron state is less than that of any homogeneous state.

Finally, we have the following picture of the energy variation for different possible states as a function of density in the layered case (Fig. 22):

for $0 < n < n_{\mathrm{c}5}$, the system is separated into FM polarons of ellipsoidal shape within an insulating AFM matrix;

for $n > n_{\mathrm{c}5}$, the system becomes an FM metal.

6. Transport properties of phase-separated manganites

In the last section of this review, we will discuss the transport properties of phase-separated manganites by applying the theoretical results obtained in previous sections. The primary transport characteristics are the behavior of resistance and magnetoresistance at low doping levels. In addition, the problem of giant $1/f$ noise will be considered. Note that the study of transport properties in materials with colossal magnetoresistance is as important as the study of superconducting characteristics in HTSCs.

6.1 Resistance in the percolation regime in phase-separated manganites

As discussed in Section 3.2, at low electron densities the system separates into FM polarons within an AFM matrix, each polaron containing one conduction electron (see Fig. 4).

When discussing the transport mechanisms in such a system, two possibilities should be considered, the motion of an FM polaron as a whole and percolation-like hops of conduction electrons from one polaron to a neighboring one. The first mechanism is ineffective, however, because of a fairly large effective mass of an FM polaron due to spins localized on it. Ferrons therefore move extremely slowly in the material. Furthermore, in real manganites ferrons are very often trapped by impurity centers (the 'pinning effect'). Thus, we are left with the percolation-like hopping of conduction electrons from ferron to ferron as the dominant mechanism.

Let us consider the first step in the percolation process. The typical situation is as shown in Fig. 23.

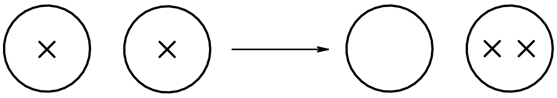

Figure 23. First percolation step in phase-separated manganites.

This step requires overcoming an energy barrier of height [56]

$$A = 2E(1) - E(2) - E(0)\,. \tag{60}$$

Note that in Eqn (60) $E(1)$ is the energy of a ferron with a single conduction electron, $E(2)$ is the same for a ferron with two electrons, and $E(0)$ is the energy of an 'empty' ferron. The lifetime of an empty ferron is assumed to be much longer than the characteristic time of electron hopping from a doubly occupied to an empty ferron. This assumption has been shown to be valid by a lifetime estimate of Ref. [56]. Without the loss of generality, we can set $E(0) = 0$. The value of $E(1)$ is determined mainly by the energy of electron delocalization within a ferron and can be estimated as

$$E(1) \sim t\,\frac{a^2}{R_{\text{pol}}^2}\,. \tag{61}$$

Expressing the polaron radius in terms of the critical concentration for the overlap of ferrons n_{c}, we obtain

$$E(1) \sim t n_{\text{c5}}^{2/3}\,, \tag{62}$$

where the density n_{c5}, as already discussed, in fact corresponds to the percolation threshold [50]. In real manganites, we have $n_{\text{c5}} \sim 0.16$, which gives $E(1) \sim 200-300$ K. Naturally, we can estimate $E(2)$ by writing

$$E(2) \sim 2E(1) + V_{\text{Coul}}\,, \tag{63}$$

where V_{Coul} is the Coulomb energy.

From this we conclude that, in order of magnitude, the energy barrier height is

$$A \sim V_{\text{Coul}} \sim \frac{e^2}{\varepsilon R_{\text{pol}}}\,, \tag{64}$$

where ε is the static dielectric constant.

In real manganites, as already discussed in Section 4, the correlation length is $r_s \gtrsim 4$, leading to A of order 1000 K. It can be seen that the physics governing transport in phase-separated manganites is similar to the elegant Coulomb blockade physics one encounters in the theory of mesoscopic phenomena [57, 58].

By analogy with the Coulomb blockade, it is clear that the system should have high resistance at temperatures $T \ll A$.

Now let us consider the second percolation step. For this, the typical situation is as shown in Fig. 24.

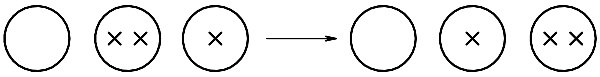

Figure 24. Second percolation step in phase-separated manganites.

At the second step, there is clearly no energy barrier to overcome. Since the same is true for all the successive percolation steps, a situation similar to that in nondegenerate semiconductors obtains: once a carrier has overcome the energy barrier, it is in the conduction band and moves freely there. Such is the qualitative picture of how polaron conduction takes place in manganites. Note that at low temperatures, $T \ll A$, and low applied voltages, $U_{\text{dc}} \ll A$, the characteristic electron hopping time for the first percolation step can be written [56] as

$$\gamma = \frac{1}{\tau} = \omega_0 \exp\left\{-\frac{r}{l} - \frac{A}{2T}\right\}, \tag{65}$$

where l is the tunneling length ($l \gtrsim 2R_{\text{pol}}$), and ω_0 is a characteristic frequency related to the rearrangement (depolarization) of the spin structure within an FM polaron. In order of magnitude, the frequency ω_0 is equal to the Fermi energy of the conduction electrons, i.e., $\omega_0 \sim \varepsilon_{\text{F}} \sim t n^{2/3}$.

The crucial point here is that the exponential $\exp(-A/2T)$ dominating Eqn (65) is associated with the Coulomb blockade. The additional exponential $\exp(-r/l)$ is of the order $\exp\left[-(n_{\text{c5}}/n)^{1/3}\right]$ and is associated with the under-barrier tunneling of a conduction electron through the insulating matrix between ferrons.

From here on, we actually ignore the AFM structure of this insulating matrix. Note that the factor $2T$ in the term $A/2T$ relates to the requirement that the detailed balance condition be met for the creation of two-electron ferrons [56].

Thus, in the limit of strong Coulomb interaction, we have

$$\frac{A}{T} \gg \left(\frac{n_{\text{c5}}}{n}\right)^{1/3} > 1\,. \tag{66}$$

This limit is opposite to the high-temperature limit $(n_{\text{c5}}/n)^{1/3} \gg A/T$ usually considered in percolation problems in doped semiconductors [59]. Physically, our limit is closer to that considered in Mott's monograph [17]. The conductivity calculation in Ref. [56] led to the following results:

$$\sigma = \frac{1}{\rho} = B\sigma_{\min}\,\frac{\omega_0}{T}\exp\left(-\frac{A}{2T}\right), \tag{67}$$

where $\sigma_{\min}$ is the minimum conductivity in our system.

It is seen that the conductivity increases with the temperature as $(1/T)\exp(-A/2T)$, a behavior typical of tunneling systems [17]. The temperature-independent coefficient B in Eqn (67), in addition to numerical factors, presumably contains the percolation exponential $\exp[-\beta/(n^{1/3}l)]$, although the authors have no rigorous mathematical proof of this. Note that, formally, formula (67) leads to a maximum in the conductivity (minimum in the resistivity) at a temperature $T = A/2$. This minimum, however, lies at the boundary of the validity range of our theory [see the inequality chain (66)].

6.2 Magnetoresistance in phase-separated manganites

Magnetoresistance is one of the most important characteristics of manganites. In this class of compounds it is usually large and negative, so that in writing the standard definition of magnetoresistance is

$$|MR| = \frac{\rho(0) - \rho(H)}{\rho(H)} = \frac{\rho(0)}{\rho(H)} - 1\,. \tag{68}$$

The modulus sign is used to account for the negative magnetoresistance in our system. Substituting for the resistance from Eqn (67), we obtain

$$|MR| = \exp\left[\frac{A(H=0) - A(H)}{2T}\right] - 1\,. \tag{69}$$

It is now necessary to determine $A(H)$. To do this, we again use the estimate (64) and write $A(H)$ in the form

$$A(H) \sim \frac{e^2}{\varepsilon R_{\mathrm{pol}}(H)}\,.$$

But, as already discussed in Section 2, the polaron radius in a magnetic field can be written as

$$R_{\mathrm{pol}}(H) \sim a\left(\frac{t}{J_{ff}^{\mathrm{eff}} S^2}\right)^{1/5},$$

where $J_{ff}^{\mathrm{eff}} S^2 = J_{ff} S^2 - g\mu_{\mathrm{B}} HS$.

Thus, in the experimentally accessible magnetic field range, $g\mu_{\mathrm{B}} HS < J_{ff} S^2$, one has

$$A(H) = A(0)[1 - bH]\,, \tag{70}$$

where $b = (1/5) g\mu_{\mathrm{B}}/(J_{ff} S)$.

From this it follows that for $T < A$ the magnetoresistance is indeed negative and that in the phase-separated region it is given by

$$|MR| = \exp\left(\frac{A}{2T}\, bH\right) - 1\,. \tag{71}$$

We emphasize that, for small magnetic fields and low temperatures, the absolute magnitude of the magnetoresistance is small:

$$|MR| = \frac{A}{2T}\, bH \ll 1\,.$$

In higher fields (but such that the condition $bH \ll 1$ still holds), as the temperature is lowered, the absolute value of magnetoresistance ultimately becomes greater than unity and starts growing exponentially:

$$|MR| = \exp\left(\frac{A}{2T}\, bH\right).$$

Note that for not very low temperatures, $T \lesssim A$, and typical values of the gyromagnetic ratio, $g \sim 10$, the absolute value of magnetoresistance in the phase-separated region becomes larger than unity only in high enough magnetic fields, $H \sim 10$ T.

The analysis presented here does not include the effects related to the dependence of scattering probability on the angle between the conduction electron spin and the magnetic moment of a droplet. These effects might lead to an exponential prefactor in Eqn (71) depending in a nontrivial way on H and T.

6.3 $1/f$ noise in phase-separated manganites

The nontrivial physics of the low-frequency $1/f$ noise occurring in many semiconductor and metallic systems has been discussed widely in the literature since the early 1980s (see Refs [60, 61] for reviews). Serious interest in $1/f$ noise in phase-separated manganites has been spurred by the experiments of Podzorov et al. [62] who observed that, even far away from the percolation threshold, the $1/f$ noise amplitude in phase-separated regions is 5 to 6 orders of magnitude larger than typically observed in semiconductor and metallic systems. We will explain this phenomenon by again considering a simple ferron model and examining how the voltage fluctuations characteristic of $1/f$ noise relate to conductivity fluctuations [56]. These latter will in turn be related to fluctuations in the number of doubly occupied (or empty) ferrons caused by ferron-to-ferron hopping of conduction electrons.

In mathematical terms, the ideology behind all this is described by the relations

$$\frac{\langle \delta U^2 \rangle_\omega}{U_{\mathrm{dc}}^2} = \frac{\langle \delta\sigma^2 \rangle_\omega}{\sigma^2} = \frac{\langle \delta n_2^2 \rangle_\omega}{\overline{n}_2^2}\,, \tag{72}$$

where $\delta\sigma$ is the conductivity fluctuation, δn_2 is the fluctuation in the number of double-electron ferrons, and $\overline{n}_2$ is the thermodynamic average of this number. The symbol $\langle \ldots \rangle_\omega$ in Eqn (72) denotes the spectral component of the quantity under study. Using the relaxation equation for the density fluctuation δn_2,

$$\delta\dot{n}_2 = -\frac{\delta n_2}{\tau(r)}\,, \tag{73}$$

where the relaxation time is again given by Eqn (65),

$$\frac{1}{\tau} = \omega_0 \exp\left(-\frac{r}{l} - \frac{A}{2T}\right),$$

we find that

$$\langle \delta n_2^2 \rangle_\omega = 8\pi\overline{n}_2 \langle \delta n_2^2 \rangle_T \int_0^\infty \frac{\tau(r)}{1 + \omega^2\tau^2(r)}\, r^2\, \mathrm{d}r\,, \tag{74}$$

where $\langle \delta n_2^2 \rangle_T = \overline{n}_2/2V_{\mathrm{s}}$ is the thermal average of the fluctuation squared in the number of double-electron ferrons, and $V_{\mathrm{s}} = L_1 L_2 L_3$ is the sample volume.

Finally,

$$\langle \delta n_2^2 \rangle_\omega = 4\pi\, \frac{\overline{n}_2^2}{V_{\mathrm{s}}} \int_0^\infty \frac{\tau(r) r^2\, \mathrm{d}r}{1 + \omega^2\tau^2(r)}\,, \tag{75}$$

and accordingly

$$\frac{\langle \delta U^2 \rangle_\omega}{U_{\mathrm{dc}}^2} = \frac{4\pi}{V_{\mathrm{s}}} \int_0^\infty \frac{\tau(r)}{1 + \omega^2\tau^2(r)}\, r^2\, \mathrm{d}r\,. \tag{76}$$

Note that the characteristic $1/f$-noise frequencies typically lie in a wide range (see Ref. [60]) defined by the inequalities

$$\tilde{\omega}_0 \exp\left(-\frac{L_{\mathrm{s}}}{l}\right) \ll \omega \ll \tilde{\omega}_0\,, \tag{77}$$

where $\tilde{\omega}_0 = \omega_0 \exp(A/2T)$, and $L_{\mathrm{s}} \sim 10^{-1} - 1$ cm is the minimal sample size. Therefore, for low temperatures $T \ll A$, we find from Eqn (76), to a logarithmic accuracy, that

$$\frac{\langle \delta U^2 \rangle_\omega}{U_{\mathrm{dc}}^2} \approx \frac{2\pi^2 l^3}{V_{\mathrm{s}}}\, \frac{1}{\omega} \ln^2\left(\frac{\tilde{\omega}_0}{\omega}\right). \tag{78}$$

Thus, over a wide low-frequency range determined by Eqn (77) the spectrum of voltage fluctuations squared is indeed of the form $1/f$. Note that the quantity which was actually measured by Podzorov and colleagues [62] was the coefficient α defined by

$$\alpha = \frac{\langle \delta U^2 \rangle_\omega V_s \omega}{U_{dc}^2} = 2\pi^2 l^3 \ln^2\left(\frac{\tilde{\omega}_0}{\omega}\right). \tag{79}$$

Note also that the characteristic frequencies in this experiment were in the range $\omega \sim 1$ Hz to 1 MHz.

Inserting typical tunneling length values $l \sim 2R_{\text{pol}} \sim 20-30$ Å into Eqn (79) and noting that at temperatures $T \lesssim A$ the quantity $\tilde{\omega}_0 \gtrsim 200$ K (i.e., $\tilde{\omega}_0 \gtrsim 2 \times 10^{13}$ Hz), we obtain $\alpha \sim 10^{-16}-10^{-17}$ cm^3. This is indeed several orders of magnitude larger than in conventional semiconductor systems (see review article [60]). The additional increase in α is due to the large value of the logarithm squared in Eqn (79). Note that, as the percolation threshold is approached, $n \to n_{c5}$, the coefficient α increases even more rapidly.

In conclusion, in this section the transport properties of separated manganites have been examined using a simplified model that neglects FM ferron moments and the properties of the insulating AFM matrix. Introducing large FM moments of neighboring ferrons into the description of the tunneling of electrons from one ferron to a neighboring one will add the beautiful physics of the so-called spin-assistant tunneling [63] to the picture. As a result, the exponential prefactor in the expressions for the conductivity, Eqn (67), and the magnetoresistance, Eqn (71), will depend on the relative orientation of the magnetic moments of neighboring ferromagnetic droplets. Also, inclusion of the interaction of a tunneling electron with the AFM fluctuations of the insulating matrix will make the problem very similar to the famous problem of tunneling with dissipation [64–66].

7. Summary

In the present review, we have attempted to describe, in a general model, the ground state and transport properties of phase-separated systems, restricting our attention to the physically transparent case of small-scale phase separation. The study of transport properties in systems with small-scale separation provides a bridge between two fields currently the most active in solid-state research, namely the physics of strongly correlated systems and mesoscopic physics. This makes phase-separated manganites very attractive for both theoretical and experimental research, as shown by the large number of publications in this area in the last two years.

Acknowledgments

We are grateful to A F Andreev, N A Babushkina, Ya M Blanter, J van den Brink, P Wölfle, D Wohlhardt, E Dagotto, D V Efremov, Yu Kagan, C Di Castro, H Kontani, F V Kusmartsev, P Littlewood, A Loidl, M S Mar'enko, M V Mostovoy, V Nolting, N M Plakida, A L Rakhmanov, L M Fisher, P Fulda, G Khaliulin, L Held, M Hennion, S-W Cheong, D Edwards, and especially É L Nagaev and D I Khomskiĭ for fruitful cooperation and useful discussions.

This work was supported by INTAS (Grants Nos 97-0963 and 97-11954) and the Russian Foundation for Basic Research (projects 00-02-16255 and 00-15-96570) as well as by the Russian Federation President's Grant No. 96-15-9694 and the Russia–Netherlands scientific cooperation program.

References

1. Jonker G H, van Santen J H *Physica* **16** 337 (1950); Jonker G H *Physica* **22** 707 (1956)
2. Wollan E O, Koehler W C *Phys. Rev.* **100** 545 (1955)
3. Jin S et al. *Science* **264** 413 (1994)
4. Nagaev É L *Usp. Fiz. Nauk* **166** 833 (1996) [*Phys. Usp.* **39** 781 (1996)]
5. Khomskii D I, Sawatzky G A *Solid State Commun.* **102** 87 (1997)
6. Ramirez A P *J. Phys.: Condens. Matt.* **9** 8171 (1997)
7. Coey J M D, Viret M, von Molnár S *Adv. Phys.* **48** 167 (1999)
8. Loktev V M, Pogorelov Yu G *Fiz. Nizk. Temp.* **26** 231 (2000) [*Low Temp. Phys.* **26** 171 (2000)]
9. Emery V J, Kivelson S A, Lin H Q *Phys. Rev. Lett.* **64** 475 (1990)
10. Zaanen J, Gunnarsson O *Phys. Rev. B* **40** 7391 (1989)
11. Castellani C, Di Castro C, Grilli M *Phys. Rev. Lett.* **75** 4650 (1995)
12. Nagaev É L *Usp. Fiz. Nauk* **165** 529 (1995) [*Phys. Usp.* **38** 497 (1995)]
13. Nagaev É L *Pis'ma Zh. Eksp. Teor. Fiz.* **6** 484 (1967) [*JETP Lett.* **6** 18 (1967)]; *Zh. Eksp. Teor. Fiz.* **54** 228 (1968) [*Sov. Phys. JETP* **27** 122 (1968)]
14. Nagaev É L *Pis'ma Zh. Eksp. Teor. Fiz.* **16** 558 (1972) [*JETP Lett.* **16** 394 (1972)]; Kashin V A, Nagaev É L *Zh. Eksp. Teor. Fiz.* **66** 2105 (1974) [*Sov. Phys. JETP* **39** 1036 (1974)]
15. Kasuya T, Yanase A, Takeda T *Solid State Commun.* **8** 1543, 1551 (1970)
16. Krivoglaz M A *Usp. Fiz. Nauk* **106** 360 (1972); **111** 617 (1973) [*Sov. Phys. Usp.* **15** 153 (1972); **16** 856 (1974)]
17. Mott N F, Davis E A *Electronic Processes in Non-Crystalline Materials* (Oxford: Clarendon Press, 1971) [Translated into Russian (Moscow: Mir, 1982)]
18. Bulaevskiĭ L N, Nagaev É L, Khomskiĭ D I *Zh. Eksp. Teor. Fiz.* **54** 1562 (1968) [*Sov. Phys. JETP* **27** 836 (1968)]
19. Uehara M et al. *Nature* **399** 560 (1999)
20. Balagurov A M et al. *Eur. Phys. J. B* **19** 215 (2001)
21. Khomskii D I *Physica B* **280** 325 (2000)
22. Jirák Z et al. *J. Magn. Magn. Mater.* **53** 153 (1985)
23. Mori S, Chen C H, Cheong S-W *Nature* **392** 473 (1998)
24. Millis A J, Littlewood P B, Shraiman B I *Phys. Rev. Lett.* **74** 5144 (1995)
25. van den Brink J, Khomskii D I *Phys. Rev. Lett.* **82** 1016 (1999); van den Brink J, Khaliulin G, Khomskii D I *Phys. Rev. Lett.* **83** 551 (1999)
26. Jackeli G, Perkins N B, Plakida N M *Phys. Rev. B* **62** 372 (2000)
27. Mutou T, Kontani H *Phys. Rev. Lett.* **83** 3685 (1999)
28. Zener C *Phys. Rev.* **82** 403 (1951)
29. Anderson P W, Hasegawa H *Phys. Rev.* **100** 675 (1955)
30. de Gennes P-G *Phys. Rev.* **118** 141 (1960)
31. Nagaev É L *Zh. Eksp. Teor. Fiz.* **57** 1274 (1969) [*Sov. Phys. JETP* **30** 693 (1970)]
32. Nagaev É L *Fizika Magnitnykh Poluprovodnikov* (Physics of Magnetic Semiconductors) (Moscow: Nauka, 1979) [Translated into English (Moscow: Mir Publ., 1983)]
33. Zaanen J, Oles A M, Horsch P *Phys. Rev. B* **46** 5798 (1992)
34. Kagan M Yu, Khomskii D I, Mostovoy M V *Eur. Phys. J. B* **12** 217 (1999)
35. Zhang F C, Rice T M *Phys. Rev. B* **37** 3759 (1988)
36. Sigrist M et al. *Phys. Rev. Lett.* **70** 2960 (1993)
37. Hubbard J *Proc. R. Soc. London Ser. A* **276** 238 (1963)
38. Verwey E J W *Nature* **144** 327 (1939); Verwey E J W, Haayman P W *Physica* **8** 979 (1941)
39. Kagan Yu, Maksimov L A *Zh. Eksp. Teor. Fiz.* **87** 348 (1984); **88** 992 (1985) [*Sov. Phys. JETP* **60** 188 (1984); **61** 545 (1985)]
40. Khomskiĭ D I, Preprint FIAN No. 105 (Moscow: FIAN, 1969)
41. Kagan M Yu, Kugel K I, Khomskii D I *Zh. Eksp. Teor. Fiz.* **120** 470 (2001) [*JETP* **93** 415 (2001)]
42. Allodi G et al. *Phys. Rev. B* **56** 6036 (1997)
43. Yakubovskii A et al. *Phys. Rev. B* **62** 5337 (2000)
44. Hennion M et al. *Phys. Rev. Lett.* **81** 1957 (1998)
45. Babushkina N A et al. *Phys. Rev. B* **59** 6994 (1999)
46. Voloshin I F et al. *Pis'ma Zh. Eksp. Teor. Fiz.* **71** 157 (2000) [*JETP Lett.* **71** 106 (2000)]

47. Moritomo Y et al. *Phys. Rev. B* **60** 9220 (1999)
48. Yunoki S, Hotta T, Dagotto E *Phys. Rev. Lett.* **84** 3714 (2000)
49. Mukhin A A et al. *Europhys. Lett.* **49** 514 (2000)
50. Gor'kov L P *Usp. Fiz. Nauk* **168** 665 (1998) [*Phys. Usp.* **41** 589 (1998)]; Gor'kov L P, Kresin V Z *Pis'ma Zh. Eksp. Teor. Fiz.* **67** 985 (1998) [*JETP Lett.* **67** 985 (1998)]
51. Fäth M et al. *Science* **285** 1540 (1999)
52. Balents L, Varma C M *Phys. Rev. Lett.* **84** 1264 (2000)
53. Barzykin V, Gor'kov L P *Phys. Rev. Lett.* **84** 2207 (2000)
54. Nagaev É L *Zh. Eksp. Teor. Fiz.* **114** 2225 (1998) [*JETP* **87** 1214 (1998)]; Nagaev E L *Phys. Rev. B* **60** 455 (1999)
55. Kagan M Yu, Mostovoy M V, Khomskii D I *Physica B* **284 – 288** 1209 (2000)
56. Rakhmanov A L, Kugel K I, Blanter Ya M, Kagan M Yu *Phys. Rev. B* **63** 174424 (2001)
57. Averin D V, Likharev K K, in *Mesoscopic Phenomena in Solids* (Eds B L Altshuler, P A Lee, R A Webb) (Amsterdam: Elsevier, 1992)
58. Beenakker C I M, Bootsma S K, in *Frontiers in Nanoscale Science of Micron/Submicron Devices* (Eds A-P Jauho, E V Buzaneva) (Dordrecht: Kluwer Acad. Publ., 1996)
59. Shklovskiĭ B I, Éfros A L *Elektronnye Svoĭstva Legirovannykh Poluprovodnikov* (Electronic Properties of Doped Semiconductors) (Moscow: Nauka, 1979) [Translated into English (Berlin: Springer-Verlag, 1984)]
60. Dutta P, Horn P M *Rev. Mod. Phys.* **53** 497 (1981)
61. Kogan Sh *Electronic Noise and Fluctuations in Solids* (Cambridge: Cambridge Univ. Press, 1996)
62. Podzorov V et al. *Phys. Rev. B* **61** R3784 (2000)
63. Tomsovic S (Ed.) *Tunneling in Complex Systems* (Singapore: World Scientific, 1998)
64. Caldeira A O, Leggett A J *Ann. Phys.* (New York) **149** 374 (1983)
65. Vladár K, Zawadowski A *Phys. Rev. B* **28** 1564 (1983)
66. Kagan Yu, Prokof'ev N V, in *Quantum Tunneling in Condensed Matter* (Eds Yu Kagan, A J Leggett) (Amsterdam: Elsevier, 1992) p. 37